arXiv:1605.07454v3 [physics.flu-dyn] 28 Nov 2016

# Subcritical convection of liquid metals in a rotating sphere using a quasi-geostrophic model

Céline Guervilly[1] and Philippe Cardin[2]

[1]School of Mathematics and Statistics, Newcastle University, Newcastle upon Tyne, NE1 7RU UK
[2]Institut des Sciences de la Terre, Université Grenoble Alpes, CNRS, 38041 Grenoble, France

November 29, 2016

**Abstract**

We study nonlinear convection in a rapidly rotating sphere with internal heating for values of the Prandtl number relevant for liquid metals ($Pr \in [10^{-2}, 10^{-1}]$). We use a numerical model based on the quasi-geostrophic approximation, in which variations of the axial vorticity along the rotation axis are neglected, whereas the temperature field is fully three-dimensional. We identify two separate branches of convection close to onset: (i) a well-known weak branch for Ekman numbers greater than $10^{-6}$, which is continuous at the onset (supercritical bifurcation) and consists of thermal Rossby waves, and (ii) a novel strong branch at lower Ekman numbers, which is discontinuous at the onset. The strong branch becomes subcritical for Ekman numbers of the order of $10^{-8}$. On the strong branch, the Reynolds number of the flow is greater than $10^3$, and a strong zonal flow with multiple jets develops, even close to the nonlinear onset of convection. We find that the subcriticality is amplified by decreasing the Prandtl number. The two branches can co-exist for intermediate Ekman numbers, leading to hysteresis ($Ek = 10^{-6}$, $Pr = 10^{-2}$). Non-linear oscillations are observed near the onset of convection for $Ek = 10^{-7}$ and $Pr = 10^{-1}$.

## 1 Introduction

Thermal convection of a Boussinesq fluid in a rotating sphere is a classical problem in fluid dynamics that has important implications for the heat transfer and generation of magnetic fields in astrophysical bodies. In the liquid core of planets, the Ekman number, $Ek$, which measures the viscous effects compared with the Coriolis force, and the Rossby number, $Ro$, which measures the nonlinear inertial effects compared with the Coriolis force, are very small, so convection is strongly influenced by the global rotation. The linear onset of thermal convection in spherical geometry for $Ek \ll 1$ and $Ek/Pr \ll 1$ (where $Pr$ is the Prandtl number, the ratio of the kinematic viscosity to thermal diffusivity of the fluid) is now well understood following the theoretical work of Roberts (1968); Busse (1970); Soward (1977); Yano (1992); Jones *et al.* (2000), confirmed by experimental studies (Carrigan & Busse, 1983; Cordero & Busse, 1992; Cardin & Olson, 1994) and numerical models (Or & Busse, 1987; Zhang, 1992; Zhang & Jones, 1993; Ardes *et al.*, 1997; Dormy *et al.*, 2004). At the linear onset, the thermal instability takes the form of columnar flows aligned with the rotation axis, whose axial vorticity has much smaller variations along the rotation axis than in the azimuthal and cylindrical radial directions to accommodate the Proudman-Taylor theorem. These convective columns drift in the azimuthal direction, analogously to Rossby waves, and are therefore called thermal Rossby waves.

The properties of nonlinear convection for small $Ek$ and $Ro$ have received considerable attention but are still not fully understood (e.g. Jones (2007); Aurnou *et al.* (2015) for a review). At the onset of instability, any infinitesimal perturbation grows exponentially until nonlinear effects saturate the growing solution. If the transition from the basic conduction state to the convection state is continuous, then we have a supercritical branch of convection (e.g. Manneville, 2004). However, in some classical problems of fluid dynamics, the nonlinearities can promote the instability rather than saturating it. This leads to a subcritical bifurcation, meaning that, once the instability develops above the linear onset, it might continue to exist when the controlling parameter is decreased below the critical value for linear instability. Subcritical behaviour has been observed in various convective systems such as double-diffusive convection (e.g. Costa *et al.*, 1981), planar convection with moderate rotation (Veronis, 1966; Bajaj *et al.*, 2002), and Bénard-Marangoni convection (e.g. Scanlon & Segel, 1967). In thermal convection in rotating spherical geometry, weakly nonlinear analyses show that the nature of the bifurcation from the basic conduction state to the thermal Rossby waves might change from supercritical to subcritical in the limit of small Ekman numbers, at least in the case of internal heating (Soward, 1977; Plaut *et al.*, 2008). However, nonlinear numerical models, which can be computed down to $Ek = O(10^{-6})$, always find that the bifurcation is supercritical (e.g. Zhang, 1992; Aubert *et al.*, 2003; Grote & Busse, 2001; Christensen, 2002; Morin & Dormy, 2004; Yadav *et al.*, 2016). This possibly means that the numerical models are not run at sufficiently small Ekman numbers to properly capture the properties of nonlinear convection for planetary cores (where $Ek = O(10^{-15})$), even near the onset of convection. Current numerical models might thus misrepresent realistic planetary convection for more vigorous thermal driving as well. The scaling laws for the global properties of convection that are derived from the numerical models (e.g. Christensen, 2002) would then not be applicable for natural objects. Furthermore, calculations are generally performed for Prandtl numbers close to unity while liquid metals have smaller $Pr$; for instance, the liquid iron in the Earth's core is thought to have $Pr \approx 10^{-1}$ (Pozzo *et al.*, 2012). Subcriticality is observed for small Prandtl numbers in planar convection with moderate rotation (Veronis, 1966; Clever & Busse, 2000), and the value of $Pr$ might be equally significant for the nature of the bifurcation at onset in rapidly-rotating spherical convection.

The objective of the present paper is to describe nonlinear convection for $Ek \ll 1$, $Ek/Pr \ll 1$ and $Ro \ll 1$ near the onset. In order to map the different hydrodynamical regimes, we carry out an extensive exploration of the parameter space. To alleviate part of the computational limitations that apply to global models of planetary cores, we use the quasi-geostrophic (QG) approximation that was developed by Busse & Or (1986) for thermal convection in the annulus geometry of Busse (1970) with curved boundaries, and subsequently used and modified for the spherical geometry by Cardin & Olson (1994); Aubert *et al.* (2003); Morin & Dormy (2004); Schaeffer & Cardin (2005); Gillet & Jones (2006); Gillet *et al.* (2007); Plaut *et al.* (2008); Calkins *et al.* (2012). The model assumes that the flow is geostrophically balanced, i.e. the Coriolis force balances the pressure gradient at leading order. By neglecting the variation of the axial vorticity along the rotation axis, we can model the flow in two dimensions. This is an important limitation to the full dynamics of rotating convection, but this exploratory study aims to inform future three-dimensional studies. The QG approximation allows us to model thermal convection for Ekman numbers as low as $10^{-8}$. Results from the numerical implementation of the QG approximation in spherical geometry have been successfully benchmarked against the asymptotic theory (Gillet & Jones, 2006; Labbé *et al.*, 2015) and 3D numerical models (Aubert *et al.*, 2003; Plaut *et al.*, 2008) for the onset of convection, and against laboratory

experiments in rotating convection (Aubert *et al.*, 2003; Gillet *et al.*, 2007) and in shear flows (Schaeffer & Cardin, 2005) for the nonlinear regime.

The main issue of the QG approximation for rotating spherical convection is that the basic temperature background has a spherical symmetry. Treating the temperature as a 2D field is therefore an unjustified approximation, although it has been successfully used in previous studies when compared with results from 3D models and laboratory experiments (Aubert *et al.*, 2003; Morin & Dormy, 2004; Gillet *et al.*, 2007; Plaut *et al.*, 2008). In the present study, we follow the work of Schaeffer & Cardin (2006) by coupling the 2D velocity to a 3D implementation of the temperature in the whole sphere. The coupling terms require interpolations from the 2D and 3D grids. The hybrid QG-3D approach can therefore only be efficient, in term of the computational time, if the temperature is solved on a 3D grid that is coarser than the 2D grid used for the velocity. This is particularly appropriate to model fluids with small Prandtl numbers, where the dissipative scale of the temperature is larger than the viscous dissipation scale. Recent studies of rapidly-rotating convection in small Prandtl number fluids have shown that the Prandtl number has a significant influence on the convection, especially on the dominant length and time scales of the flow (Gillet *et al.*, 2007; Calkins *et al.*, 2012; King & Aurnou, 2013). In this paper, we vary $Pr$ between $[10^{-2}, 10^{-1}]$. Note that for small Prandtl numbers, convection cells attached to the equator of the outer sphere are preferred to thermal Rossby waves at the linear onset of convection when the Ekman number is moderately small (Zhang & Busse, 1987; Busse & Simitev, 2004; Plaut & Busse, 2005; Sánchez *et al.*, 2016). In the limit $Ek \ll 1$ and $Ek/Pr \ll 1$, the critical Rayleigh number at the onset of these equatorially-attached modes scales as $Ek^{-2}$, while the critical Rayleigh number at the onset of the thermal Rossby waves scales as $Ek^{-4/3}$ (Busse & Simitev, 2004). The equatorially-attached modes are therefore unlikely to occur in the Earth's core. The 3D numerical simulations of Ardes *et al.* (1997) show that the thermal Rossby waves are preferred for $Ek \leq 10^{-4}$ when $Pr = 10^{-1}$ and $Ek \leq 10^{-6}$ when $Pr = 10^{-2}$. The equatorially-attached modes are outside the scope of this paper, so we restrict our study to this range of small Ekman numbers.

For simplicity, we consider only thermal convection in a full sphere without a solid inner core to avoid the singularity of the QG approach at the tangent cylinder. Consequently, the thermal convection is driven by an homogenous internal heating, which is a well-studied variation of the classical problem of thermal convection in a rapidly-rotating sphere (Jones *et al.*, 2000), and is relevant for the early history of the Earth's core (e.g. Olson, 2013).

The layout of the paper is as follows. First, we derive the formulation of the hybrid QG-3D model that describes thermal convection in a rapidly rotating sphere in §2. Then in §3, we discuss the results from the nonlinear simulations carried out near the onset for small Ekman numbers. Subcritical convection, hysteresis and nonlinear oscillations are reported. A discussion of the results is given in §4. In Appendix A, the results at the linear onset of convection obtained with our hybrid model are compared with results from the asymptotic theory and from previous quasi-geostrophic and 3D numerical models.

## 2 Formulation of the model

We study thermal Boussinesq convection in a rotating sphere driven by internal heating. The system rotates at a constant angular velocity $\Omega \boldsymbol{e}_z$. The acceleration due to gravity is radial and linear, $\boldsymbol{g} = g_0 r \boldsymbol{e}_r$. The radius of the sphere is $r_o$ and no inner core is present. The fluid has kinematic viscosity $\nu$, thermal diffusivity $\kappa$, density $\rho$, heat capacity at constant pressure $C_p$, and thermal expansion coefficient $\alpha$, all of which are constant. We consider an homogeneous internal volumetric heating $S$. In the absence of convection, the

static temperature profile $T_s$ is calculated by solving the diffusive heat equation and can be written as

$$T_s(r) = T_o + \frac{S}{6\kappa\rho C_p}(r_o^2 - r^2), \tag{1}$$

where $T_o$ is the imposed temperature at the boundary, $r = r_o$. The governing equations are solved in dimensionless form, obtained by scaling lengths with $r_o$, times with $r_o^2/\nu$, and temperature with $\nu S r_o^2/(6\rho C_p \kappa^2)$. The system of dimensionless equations is:

$$\frac{\partial \mathbf{u}}{\partial t} + (\mathbf{u}\cdot\boldsymbol{\nabla})\,\mathbf{u} + \frac{2}{Ek}\mathbf{e}_z \times \mathbf{u} = -\boldsymbol{\nabla} p + \boldsymbol{\nabla}^{\mathbf{2}}\mathbf{u} + Ra\Theta\mathbf{r}, \tag{2}$$

$$\nabla\cdot\mathbf{u} = 0, \tag{3}$$

$$\frac{\partial \Theta}{\partial t} + \mathbf{u}\cdot\nabla\Theta - \frac{2}{Pr} r u_r = \frac{1}{Pr}\nabla^2\Theta, \tag{4}$$

where $\mathbf{u}$ is the velocity field, $p$ the modified pressure, which includes the centrifugal potential, and $\Theta$ the temperature perturbation relative to the static temperature (1).

The dimensionless numbers are, the Ekman number,

$$Ek = \frac{\nu}{\Omega r_o^2}, \tag{5}$$

the Rayleigh number,

$$Ra = \frac{\alpha g_0 S r_o^6}{6\rho C_p \nu \kappa^2}, \tag{6}$$

and the Prandtl number,

$$Pr = \frac{\nu}{\kappa}. \tag{7}$$

At $r = r_o$, the boundary condition for the velocity is no-slip and impenetrable and the temperature is fixed,

$$\mathbf{u} = \mathbf{0}, \quad \Theta = 0 \text{ at } r = r_o. \tag{8}$$

We detail below the quasi-geostrophic formulation used to model the velocity field, the 3D model used for temperature, and the numerical method. Throughout this paper, we use both spherical coordinates $\boldsymbol{u} = (u_r, u_\theta, u_\phi)$ and cylindrical polar coordinates $\boldsymbol{u} = (u_s, u_\phi, u_z)$.

### 2.1 Governing equation for the non-axisymmetric flow

We seek to model the system of equations (2)-(4) for small Ekman numbers. We choose the quasi-geostrophic (QG) approximation to model the evolution of the velocity field (Or & Busse, 1987; Brummell & Hart, 1993; Cardin & Olson, 1994; Plaut & Busse, 2002; Aubert *et al.*, 2003; Jones *et al.*, 2003; Morin & Dormy, 2004; Schaeffer & Cardin, 2005; Gillet & Jones, 2006; Calkins *et al.*, 2012; Teed *et al.*, 2012). The QG approximation reduces the three-dimensional system to a two-dimensional system by taking advantage of the small variation of the flow along $z$ due to the rapid rotation (Gillet & Jones, 2006). This approximation is only justified in the case of small slope of the boundaries, such as the Busse (1970) annulus. In the case of a sphere, the approximation is therefore not rigorously justified in any asymptotic limit. Consequently, the QG model is intended as a simplified model of convection in a rapidly rotating sphere that allows us to investigate unexplored regions of the parameter space. When possible, comparisons with theoretical, experimental and 3D numerical models show that the QG model correctly reproduces key

properties of the full system (Aubert *et al.*, 2003; Morin & Dormy, 2004; Gillet & Jones, 2006; Gillet *et al.*, 2007; Plaut *et al.*, 2008).

The QG model assumes that the fluid dynamics is dominated by the geostrophic balance, i.e. the Coriolis force balances the pressure gradient. The geostrophic velocity $\mathbf{u}^g$ is invariant along $z$ and $\mathbf{u}^g = (u_s^g, u_\phi^g, 0)$ in cylindrical polar coordinates. By taking the $z$-component of the curl of the momentum equation (2) and averaging it along $z$, we obtain the equation for the axial vorticity, $\zeta^g = (\boldsymbol{\nabla} \times \mathbf{u}^g) \cdot \boldsymbol{e}_z$,

$$\frac{\partial \zeta^g}{\partial t} + (\mathbf{u}^g \cdot \boldsymbol{\nabla})\, \zeta^g - \left( \frac{2}{Ek} + \zeta^g \right) \left\langle \frac{\partial u_z}{\partial z} \right\rangle = \nabla_e^2 \zeta^g - Ra \left\langle \frac{\partial \Theta}{\partial \phi} \right\rangle, \tag{9}$$

with

$$\nabla_e^2 A \equiv \frac{1}{s} \frac{\partial}{\partial s} \left( s \frac{\partial A}{\partial s} \right) + \frac{1}{s^2} \frac{\partial^2 A}{\partial \phi^2}, \tag{10}$$

and

$$\langle A \rangle \equiv \frac{1}{2H} \int_{-H}^{+H} A dz, \tag{11}$$

where $H = \sqrt{1 - s^2}$ is the axial distance from the spherical boundary to the equatorial plane.

The axial velocity $u_z$ is assumed to be linear in $z$. Three-dimensional linear convection models with internal heating show that the variation in $z$ of $u_z$ is not exactly linear, but it is a reasonable assumption because the variations in $z$ with respect to the linear profile are small compared with the variations in $s$ and $\phi$ (Gillet & Jones, 2006).

The velocity $\mathbf{u}^g$ can be described by a streamfunction $\psi$ that describes the non-axisymmetric (i.e. $\phi$-dependent) geostrophic flow with the addition of an axisymmetric azimuthal flow,

$$\mathbf{u}^g = \frac{1}{H} \boldsymbol{\nabla} \times (H \psi \boldsymbol{e}_z) + \overline{u_\phi^g} \boldsymbol{e}_\phi, \tag{12}$$

where

$$\overline{A} \equiv \frac{1}{2\pi} \int_0^{2\pi} A d\phi. \tag{13}$$

This choice for the streamfunction implies that the divergence of $\mathbf{u}^g$ in the equatorial plane is non-zero because of the return axial flow due to the slope of the boundaries,

$$\boldsymbol{\nabla}_e \cdot \mathbf{u}^g = -\beta u_s^g, \tag{14}$$

where

$$\boldsymbol{\nabla}_e \cdot \boldsymbol{A} \equiv \frac{1}{s} \frac{\partial s A_s}{\partial s} + \frac{1}{s} \frac{\partial A_\phi}{\partial \phi}, \tag{15}$$

and

$$\beta = \frac{1}{H} \frac{dH}{ds} = -\frac{s}{H^2}. \tag{16}$$

The third term on the left-hand side of equation (9) requires us to determine $u_z$ at the boundary $z = \pm H$:

$$u_z|_{\pm H} = \pm \frac{1}{H}\, \mathbf{u} \cdot \mathbf{n}|_{\pm H} \pm \beta H u_s^g, \tag{17}$$

where the normal vector at the boundary is $\boldsymbol{n} = \boldsymbol{e}_r$. The normal component, $\mathbf{u} \cdot \mathbf{n}|_{\pm H}$, is the Ekman pumping induced by the viscous boundary layer and is determined by asymptotic methods (Greenspan, 1968),

$$\mathbf{u} \cdot \mathbf{n}|_{z=\pm H} = -\frac{Ek^{1/2}}{2} \mathbf{n} \cdot \boldsymbol{\nabla} \times \left( \frac{\mathbf{n} \times \mathbf{u} \pm \mathbf{u}}{\sqrt{|\mathbf{n} \cdot \mathbf{e_z}|}} \right) = Ek^{1/2} P(s, u_s^g, u_\phi^g). \tag{18}$$

This analytical formulation is valid for a linear Ekman layer and for variations of the velocity that are slower than the rotation period and on larger lengthscales than $O(Ek^{1/2})$. The function $P$ is derived for a spherical boundary in Schaeffer & Cardin (2005).

Our numerical code solves the equation for the evolution of the non-axisymmetric streamfunction

$$\frac{\partial}{\partial t}\mathcal{L}\psi + (\mathbf{u}^g \cdot \boldsymbol{\nabla}_e)\,\mathcal{L}\psi - \left(\frac{2}{Ek} + \mathcal{L}\psi\right)\left(\frac{Ek^{1/2}P}{2H^2} + \beta u_s^g\right) = \nabla_e^2 \mathcal{L}\psi - Ra\left\langle \frac{\partial \Theta}{\partial \phi}\right\rangle, \tag{19}$$

where

$$\mathcal{L}\psi = \zeta^g = -\nabla_e^2\psi + \frac{1}{s}\frac{\partial}{\partial s}\left(\frac{s^2\psi}{H^2}\right). \tag{20}$$

The no-slip and impenetrable boundary conditions imply that

$$\psi = \frac{\partial \psi}{\partial s} = 0 \text{ at } s = 1. \tag{21}$$

At the centre of the sphere, the solution must be regular. Using a decomposition in Fourier modes,

$$\psi(s,\phi,t) = \sum_{m=1}^{+\infty} \hat{\psi}^m(s,t)e^{im\phi}, \tag{22}$$

the regularity condition is

$$\hat{\psi}^m = O(s^m) \text{ at } s = 0. \tag{23}$$

## 2.2 Governing equation for the zonal flow

In our model, the streamfunction $\psi$ only describes the non-axisymmetric motions, so the axisymmetric azimuthal flows, or zonal flows, are treated separately. We take the $\phi$- and $z$-averages of the $\phi$-component of the momentum equation to obtain

$$\frac{\partial \overline{u_\phi^g}}{\partial t} + \overline{u_s^g \frac{\partial u_\phi^g}{\partial s}} + \overline{\frac{u_s^g u_\phi^g}{s}} + \frac{2}{Ek}\langle \overline{u_s}\rangle = \nabla^2 \overline{u_\phi^g} - \overline{\frac{u_\phi^g}{s^2}}. \tag{24}$$

Note that the geostrophic balance imposes that $\overline{u_s^g} = 0$. The fourth term on the left-hand side of (24) involves the $z$-dependent radial velocity, which corresponds to the Ekman pumping term. Using the incompressibility of the fluid, it can be shown (Aubert *et al.*, 2003) that

$$\langle \overline{u_s}\rangle = \frac{Ek^{1/2}}{2H^{3/2}}\overline{u_\phi^g}. \tag{25}$$

The no-slip boundary condition at the outer sphere implies

$$\overline{u_\phi^g} = 0 \text{ at } s = 1. \tag{26}$$

By symmetry at the centre,

$$\overline{u_\phi^g} = 0 \text{ at } s = 0. \tag{27}$$

### 2.3 Governing equation for the temperature

The dimensionless equation for the evolution of the temperature perturbation in 3D is

$$\frac{\partial \Theta}{\partial t} + \mathbf{u}^{3d} \cdot \boldsymbol{\nabla} \Theta = \frac{1}{Pr} \left( 2 r u_r^{3d} + \nabla^2 \Theta \right). \tag{28}$$

where $\mathbf{u}^{3d}$ is the velocity in 3D. In cylindrical polar coordinates,

$$\mathbf{u}^{3d} = (u_s^g, u_\phi^g, Ek^{1/2} z P + \beta z u_s^g). \tag{29}$$

The temperature is fixed at the outer boundary so

$$\Theta = 0 \text{ at } r = 1. \tag{30}$$

At the centre, the heat flux of the spherically averaged temperature perturbation is zero,

$$\left\langle \frac{\partial \Theta}{\partial r} \right\rangle_{\mathcal{S}} = \int_{\mathcal{S}} \frac{\partial \Theta}{\partial r} d\mathcal{S} = 0 \text{ at } r = 0, \tag{31}$$

where $\mathcal{S}$ is a spherical surface. By symmetry, the non-spherically symmetric components of $\Theta$ are zero,

$$\Theta - \langle \Theta \rangle_{\mathcal{S}} = 0 \text{ at } r = 0. \tag{32}$$

### 2.4 Numerical method

In summary, the governing equations of our hybrid quasi-geostrophic-3D model are

$$\frac{\partial}{\partial t} \mathcal{L}\psi + (\mathbf{u} \cdot \boldsymbol{\nabla}_e) \mathcal{L}\psi - \left( \frac{2}{Ek} + \mathcal{L}\psi \right) \left( \frac{Ek^{1/2} P}{2H^2} + \beta u_s \right) = \nabla_e^2 \mathcal{L}\psi - Ra \left\langle \frac{\partial \Theta}{\partial \phi} \right\rangle, \tag{33}$$

$$\frac{\partial \overline{u_\phi}}{\partial t} + \overline{u_s \frac{\partial u_\phi}{\partial s}} + \frac{\overline{u_s u_\phi}}{s} + \frac{\overline{u_\phi}}{Ek^{1/2} H^{3/2}} = \nabla^2 \overline{u_\phi} - \frac{\overline{u_\phi}}{s^2}, \tag{34}$$

$$\frac{\partial \Theta}{\partial t} + \mathbf{u}^{3d} \cdot \boldsymbol{\nabla} \Theta = \frac{1}{Pr} \left( 2 r u_r^{3d} + \nabla^2 \Theta \right), \tag{35}$$

subject to the boundary conditions (21), (23), (26)-(27), (30)-(32), and the 3D velocity used in the temperature equation is given by equation (29). The superscripts $g$ have been removed for clarity.

Equations (33) and (34) are solved on a two dimensional grid in the equatorial plane. A second-order finite difference scheme is implemented in radius with irregular spacing (finer near the outer boundary). In the azimuthal direction, the streamfunction and zonal velocity are expanded in Fourier modes. Equation (35) is solved on a three dimensional grid. Similarly to the 2D grid, a finite difference scheme is used in radius. The temperature is expanded in spherical harmonics $Y_l^m$ in the angular coordinates with $l$ representing the latitudinal degree and $m$ the azimuthal mode. This allows for a simple implementation of the boundary conditions at the centre. A Crank-Nicolson scheme is implemented for the time integration of the diffusion terms and an Adams-Bashforth procedure is used for the other terms. Our hybrid approach is numerically efficient compared with a fully 3D approach when considering small Prandtl numbers, i.e. when the diffusion of the temperature happens on shorter timescales than the viscous dissipation. In this case, the 3D grid of the temperature requires less radial points and azimuthal modes than the 2D grid of the velocity, so smaller gridsteps and timestep can be used for the velocity. The most

demanding nonlinear simulations were run at $Ek = 10^{-8}$. The numerical resolution required to resolve the simulation run at $Ek = 10^{-8}$ and $Pr = 10^{-1}$ for the largest Rayleigh number ($Ra \approx 6Ra_c$) is 1600 radial points, 300 Fourier modes $m$ for the 2D velocity grid and 800 radial points, 200 degrees $l$ and 200 modes $m$ of the spherical harmonics for the 3D temperature grid.

The buoyancy term in equation (33) requires the integration of the temperature along $z$ for each point of coordinates $(s, \phi)$ on the 2D grid at each timestep. To do so, we use a linear interpolation in $r$ and $\theta$ from the 3D spherical grid onto a 3D cylindrical projection of the velocity grid. The spectral decomposition in $\phi$ for the velocity and temperature allows a straightforward interpolation in spectral space. To calculate the 3D velocity used for the advection of temperature, we use a linear interpolation in $s$. Again, the interpolation in $\phi$ is straightforward in spectral space.

In order to benchmark the numerical model, we performed calculations with the linearised version of the code to determine the critical parameters at the linear onset of convection. The linear results are given in Appendix A and compared with results from the asymptotic theory and from published numerical studies using either a 3D or a QG model. The comparison shows that our numerical results tend to the asymptotic values as the Ekman number decreases. In the following, the critical Rayleigh number at the linear onset of convection calculated with our numerical code is denoted $Ra_c$.

### 2.5 Definition of the output parameters

To quantify the global properties of convection, we use the following quantities calculated from the output of the simulations. In our dimensionless units, the Reynolds number corresponds to the root mean square (rms) value of the velocity,

$$Re^*(t) = \left( \frac{3}{4\pi} \int_0^{2\pi} \int_0^1 (u_s^2(s,\phi,t) + u_\phi^2(s,\phi,t)) 2H(s) s ds d\phi \right)^{1/2}, \tag{36}$$

and

$$Re = \frac{1}{\Delta t} \int_{\Delta t} Re^*(t) dt, \tag{37}$$

where $u_\phi$ includes the zonal velocity. We measure the convective Reynolds number, $Re_c^*$, as in equation (36) but including only the non-axisymmetric velocity. Its time average is denoted $Re_c$. Similarly, we measure the zonal Reynolds number, $Re_0^*$, including only the axisymmetric velocity, and its time average is denoted $Re_0$. The time averages are calculated over a long period of time after the system reaches a statistical equilibrium.

We define the radial profile of the time-averaged zonal velocity as

$$U_0(s) = \frac{1}{\Delta t} \int_{\Delta t} \overline{u_\phi}(s,t) dt, \tag{38}$$

and the radial profile of the rms radial velocity,

$$U_s(s) = \frac{1}{\Delta t} \int_{\Delta t} \left( \frac{1}{2\pi s} \int_0^{2\pi} u_s^2(s,\phi,t) s d\phi \right)^{1/2} dt. \tag{39}$$

The Nusselt number, which is the ratio of the total heat flux, $Q_t$, to the conductive heat flux $Q_\kappa$, is often used to measure the efficiency of the convective heat transport. In a convective system with internal heating and fixed temperature boundaries, the mean total outward heat flux must balance heat production, so $Q_t = r_o S/3$. To estimate the

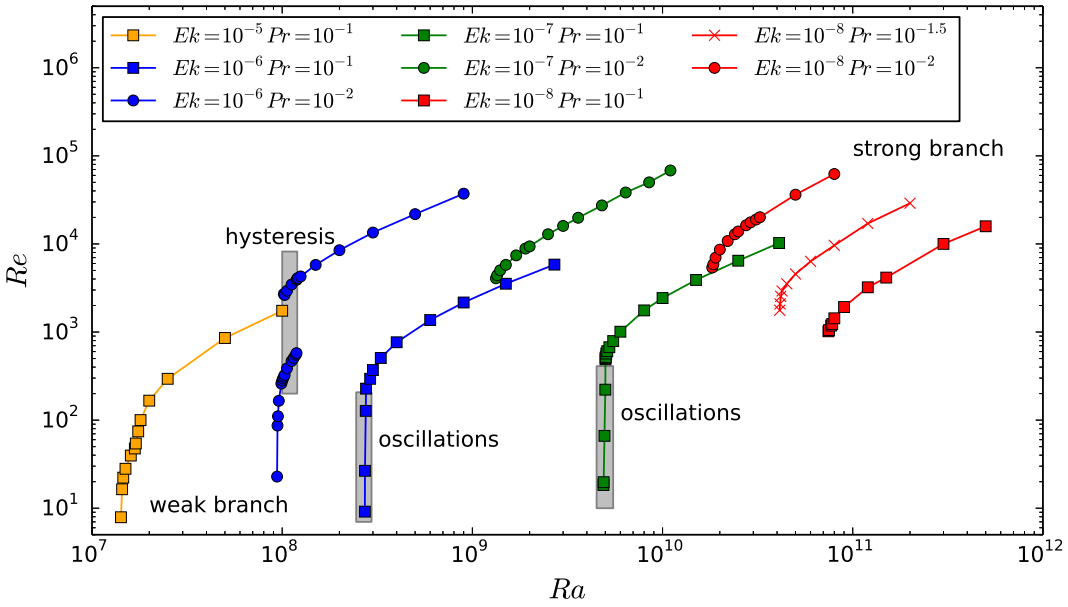


Figure 1: Time-averaged values of the Reynolds number, $Re$, as a function of the Rayleigh number for different $Ek$ (identified by different colours) and $Pr$ (different symbols). The annotations correspond to the different regimes discussed in §3.

heat flux that is conducted along the spherically averaged temperature gradient, we define the equivalent internal heating, $S_{eq}$, that would correspond to the purely conductive state with a temperature at the centre $T_c = T_s(r=0) + \langle\Theta(r=0)\rangle_{\mathcal{S}}$, where $\langle\Theta(r=0)\rangle_{\mathcal{S}}$ is an output of the simulation. Assuming that $Q_\kappa = r_o S_{eq}/3$, we can define the Nusselt number, $Nu$, as

$$Nu = \frac{Q_t}{Q_\kappa} = \frac{S}{S_{eq}} = \frac{1}{PrT_c}, \tag{40}$$

where $S_{eq} = PrT_cS$ and $T_c = Pr^{-1} + \langle\Theta(r=0)\rangle_{\mathcal{S}}$. The decrease of the temperature at the centre due to convection is thus a good measure of the efficiency of the convective heat transport (Goluskin, 2016). We find that longer time integrations are required to ensure the saturation of $Nu$ than for the saturation of the kinetic energy.

We also measure the rms value of the axisymmetric temperature perturbation as

$$\Theta_0^*(t) = \left(\frac{3}{2}\int_0^1\int_0^\pi \overline{\Theta}^2 r^2 \sin\theta dr d\theta\right)^{1/2}. \tag{41}$$

## 3 Non-linear calculations near the onset of convection

The data set presented in this paper contains approximately 120 simulations performed at small Ekman numbers, $Ek \in [10^{-8}, 10^{-5}]$, and small Prandtl numbers, $Pr \in [10^{-2}, 10^{-1}]$. The focus of the study is convection near the onset, so the Rayleigh number has been varied up to 10 times above the critical value at the onset of convection. The values of the critical Rayleigh number at the linear onset, $Ra_c$, are given in table 2 in Appendix A for different $Ek$ and $Pr$.

To give an overview of the simulations and the results, figure 1 shows the Reynolds number, $Re$, as a function of the Rayleigh number for the different Ekman numbers (identified by different colours) and Prandtl numbers (different symbols). $Re$ reaches values up

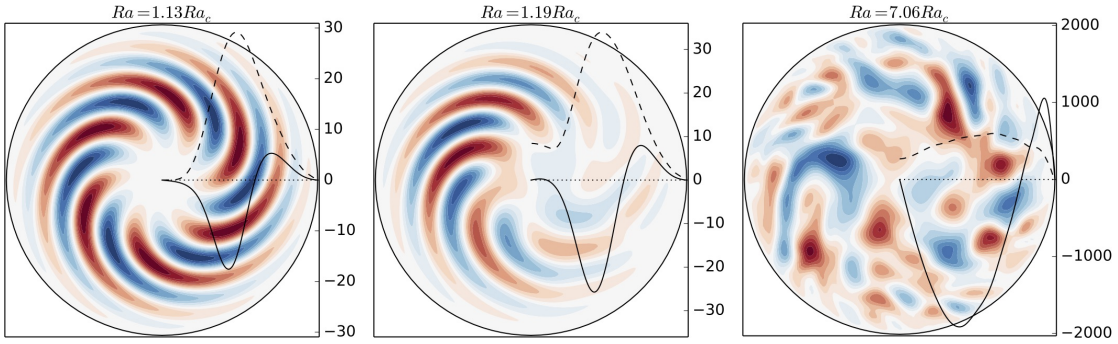


(a) (b) (c)

Figure 2: Snapshots of the streamfunction for $Ek = 10^{-5}$ and $Pr = 10^{-1}$ for (a) $Ra = 1.13Ra_c$, (b) $Ra = 1.19Ra_c$ and (c) $Ra = 7.06Ra_c$. The time-averaged radial profiles of the zonal velocity, $U_0$, (solid line) and the rms radial velocity, $U_s$, (dashed line) are plotted according to the axis on right-hand side.

to $10^5$ for the lowest Ekman and Prandtl numbers. Note that the local Rossby number, defined as the rotation period to the convective turnover time, is smaller than unity at all lengthscales in all of our simulations, in accordance with our approximation that the vortices are columnar at all scales (e.g. Nataf & Schaeffer, 2015). At moderate Ekman numbers ($Ek = 10^{-5}$), we recover results previously described in the literature, such as the sequence of bifurcations between quasi-steady and time-dependent convection. This is discussed in §3.1. In §3.2, we describe a novel branch of convection and the occurrence of subcritical convection at low $Ek$ ($Ek = 10^{-8}$). The bridge between previous results at $Ek = 10^{-5}$ and the new hydrodynamical regime at lower Ekman numbers is made at intermediate Ekman numbers ($Ek = 10^{-7} - 10^{-6}$), where we observe interesting behaviours: a hysteresis loop (described in §3.3) and nonlinear oscillations (§3.4). These different behaviours are annotated in figure 1.

### 3.1 Supercritical convection for $Ek = 10^{-5}$

We begin our study with simulations performed at $Ek = 10^{-5}$ and $Pr = 10^{-1}$ in order to link the results obtained with our hybrid QG-3D model to previous studies using either 3D or QG models.

For this Ekman number, the bifurcation from the basic conduction state is supercritical at $Ra = Ra_c$. For values of $Ra$ just above $Ra_c$, the convective flow consists of a thermal Rossby wave, a well-known flow pattern in rotating convection (e.g. Busse, 1970). Figure 2(a) shows a snapshot of the streamfunction (colour) for $Ra = 1.13Ra_c$. The linear thermal Rossby wave develops around the radius $s \approx 0.5$ and propagates eastward. For small Prandtl numbers, the thermal Rossby wave has a large tilt in the equatorial cross-section (Zhang, 1992).

Figure 3(a) shows the evolution of $Re$ as a function of the normalised Rayleigh number, $Ra/Ra_c - 1$. For $Ra/Ra_c < 1.2$, the evolution of $Re$ with $Ra/Ra_c - 1$ can be approximated by a power law $Re \sim (Ra/Ra_c - 1)^{0.42}$. A sudden transition occurs at $Ra/Ra_c = 1.2$, after which the slope of the curve becomes steeper. Around this transition, or kink, the convection changes from quasi-steady to time-dependent. The sequence of bifurcations that follows the kink has been previously documented in both 3D models (Zhang, 1992; Sun *et al.*, 1993; Tilgner & Busse, 1997; Grote & Busse, 2001; Simitev & Busse, 2003) and

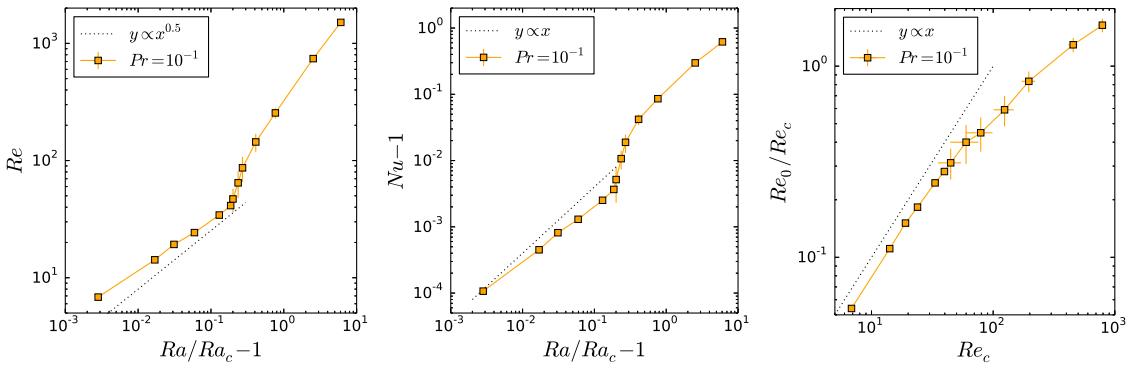


Figure 3: Evolution of the global properties of convection for $Ek = 10^{-5}$ and $Pr = 10^{-1}$. The vertical and horizontal error bars represents the standard deviation in the time series.

QG models (Schnaubelt & Busse, 1992; Morin & Dormy, 2004). Our hybrid QG model reproduces this sequence: periodic vacillations ($Ra = 1.18Ra_c$), chaotic fluctuations with a localisation of the convection ($Ra = 1.19Ra_c$, figure 2(b)), and bursts of convection ($Ra = 1.21Ra_c$). These various states are attributed to the interactions of the zonal flow and the axisymmetric temperature with the convective columns (Teed *et al.*, 2012). Interestingly, Morin & Dormy (2004) find that the kink occurs closer to the onset of convection as the Ekman number decreases, implying that quasi-steady convection in the form of thermal Rossby waves is expected to occur within a vanishingly small range of Rayleigh numbers for $Ek \to 0$. For higher Rayleigh number, the time dependence of the convection becomes irregular. Figure 2(c) shows the streamfunction for $Ra = 7.06Ra_c$. The thermal Rossby wave is no longer visible and the velocity comprises a wide range of lengthscales.

The kink at $Ra = 1.2Ra_c$ is also clearly visible in the plot of $Nu$ as a function of $Ra/Ra_c - 1$ shown in figure 3(b). Near the onset, Busse & Or (1986) predicted that the evolution of the convective heat transport with the Rayleigh number follows a power law $Nu \sim Ra/Ra_c - 1$, which has later been confirmed by Gillet & Jones (2006) with numerical results for $Pr > 1$. For $Ra < 1.2Ra_c$, our numerical results can be approximated by a power law of weaker exponent, 0.88. The slow increase of $Nu$ with the Rayleigh number for $Pr < 1$ was previously observed by Gillet & Jones (2006). After the kink, we have too few numerical points to determine whether the points still follow a power law.

In figure 2(a), we plot the time-averaged radial profile of the zonal velocity, $U_0$, for $Ra = 1.13Ra_c$. Zonal flows are produced from the nonlinear interactions of the non-axisymmetric velocity components (eq. (34)). The production of zonal flow by thermal Rossby waves has been extensively studied in the literature (e.g. Busse & Hood, 1982; Plaut *et al.*, 2008). In spherical geometry, the divergence of the Reynolds stresses produces a retrograde zonal jet in the central part and a prograde jet in the outer part. The correlation of the velocity components is caused by the tilt of the thermal Rossby waves. Figure 2(c) shows $U_0$ for $Ra = 7.06Ra_c$. The zonal flow still has a double jet structure with a prograde jet on the outer part. The peak velocity of the zonal flow is three times larger than the maximum of the radial profile of the rms radial velocity, $U_s$, also shown in the figure.

Weakly nonlinear analysis predicts that the amplitude of the zonal flow scales as the square of the amplitude of the convective velocity (Busse & Hood, 1982). Figure 3(c) shows

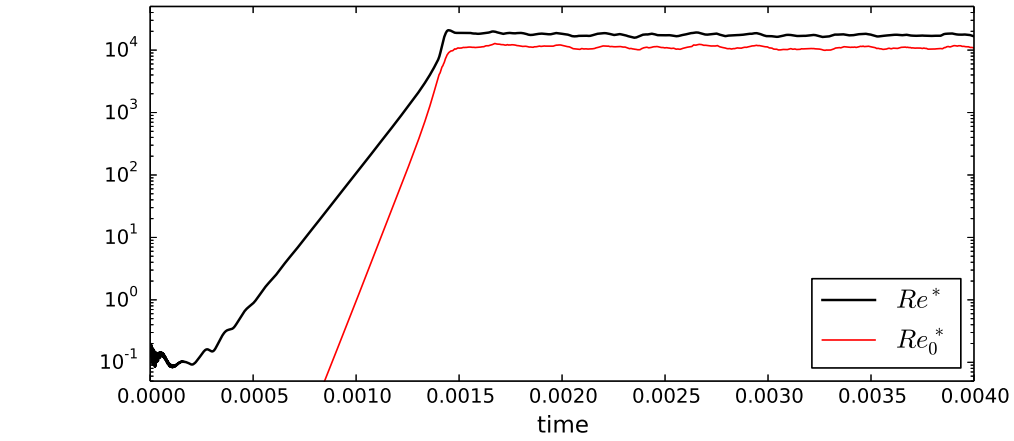


(a)

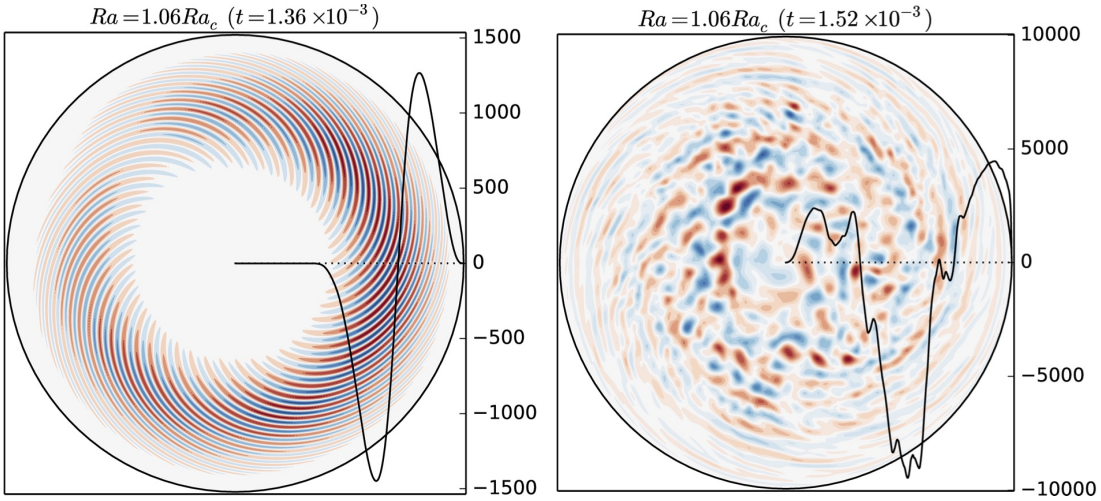


(b) (c)

Figure 4: (a) Time series of $Re^*$ (thick black line) and $Re_0^*$ (red) for $Ek = 10^{-8}$, $Pr = 10^{-2}$ and $Ra = 1.06Ra_c$. (b)-(c) Streamfunction (colour, snapshot) and radial profiles of the zonal velocity (snapshot, solid line, plotted according to the right-hand side axis) during (b) the growing phase at $t = 1.36 \times 10^{-3}$ and (c) the saturated phase at $t = 1.52 \times 10^{-3}$.

the ratio $Re_0/Re_c$ as a function of the convective velocity $Re_c$. This ratio varies linearly with $Re_c$ just above the onset, in agreement with the weakly nonlinear analysis. After the transition from quasi-steady convection to time-dependent convection, the evolution of $Re_0/Re_c$ with $Re_c$ departs from the weakly nonlinear prediction and the slope becomes shallower. The transition occurs when $Re_0$ becomes comparable to $Re_c$, in agreement with the idea that the bifurcation to time-dependent convection is due to the presence of zonal flows.

### 3.2 Subcritical convection for $E = 10^{-8}$

We now present results obtained at the small Ekman numbers that are out of reach of earlier and recent 3D models (e.g. Yadav *et al.*, 2016).

Figure 4(a) shows the time series of the Reynolds number, $Re^*$, and the zonal Reynolds number, $Re_0^*$, for $Ek = 10^{-8}$, $Pr = 10^{-2}$ and $Ra = 1.06Ra_c$. After a small temperature perturbation is added at $t = 0$, the kinetic energy grows exponentially and eventually

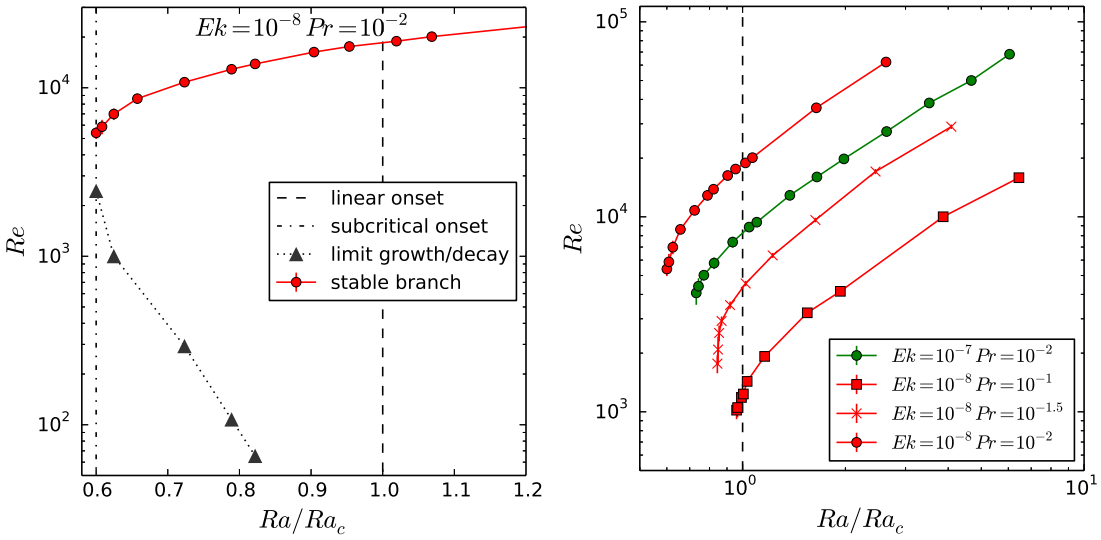


(a) (b)

Figure 5: (a) $Re$ as a function of $Ra/Ra_c$ for $Ek = 10^{-8}$ and $Pr = 10^{-2}$. The limit between the initial value of $Re^*$ leading to either the decay or the growth of the solution is plotted as triangles. (b) Same as (a) for all the cases of subcritical convection ($Ek = 10^{-8}$, $Pr \in [10^{-2}, 10^{-1}]$ and $Ek = 10^{-7}$, $Pr = 10^{-2}$).

saturates around a mean value. Despite the proximity to the onset of convection, the values of the Reynolds numbers are large in the saturated phase, on average $Re \approx 15200$ and $Re_0 \approx 9600$. Figures 4(b) and 4(c) show snapshots of the streamfunction during the growing phase and the saturated phase respectively. During the growth, the flow has the distinctive pattern of a thermal Rossby wave. The azimuthal modulation of the non-axisymmetric pattern is caused by the interaction of Rossby waves of different azimuthal wavenumbers. A snapshot of the zonal flow is also shown as a solid black line. The zonal flow has the familiar double jet structure seen at the onset of convection at $Ek = 10^{-5}$ (figure 2(a)). During the saturated phase, the flow is markedly different. The flow is now organised into two regions in the equatorial plane. In the inner region ($s < 0.6$), the pattern of the thermal Rossby waves is lost and the convective flow is vigorous with a wide range of lengthscales. In the outer part ($s > 0.6$), the velocity has a smaller amplitude and the characteristic elongated and tilted pattern of the Rossby waves is visible. This type of zonation of the convection was previously described by Sumita & Olson (2000); Aubert *et al.* (2003); Miyagoshi *et al.* (2010) for Rayleigh numbers several times above critical. In the outer part, the vortex stretching term due to the slope of the boundaries is predominant over the other forces, so Rossby waves are easily excited there. The zonal flow is also modified: its radial structure is more complex with three main jets of similar radial widths, where a jet is defined by a zonal velocity of same sign. The innermost and outermost jets remain prograde while the middle jet is retrograde. The outermost prograde zonal jet is driven by the Reynolds stresses from the tilted thermal Rossby waves in the outer region.

Figure 5(a) shows the values of $Re$ when the Rayleigh number is varied around the onset of convection for $Ek = 10^{-8}$ and $Pr = 10^{-2}$. As previously noted in figure 4(a), $Re$ becomes large (of the order of $10^4$) when $Ra$ is only just slightly increased above $Ra_c$. Remarkably, when the Rayleigh number is decreased during a simulation from $Ra \geq Ra_c$ to $Ra < Ra_c$, the convection does not decay and remains vigorous up to a value of the

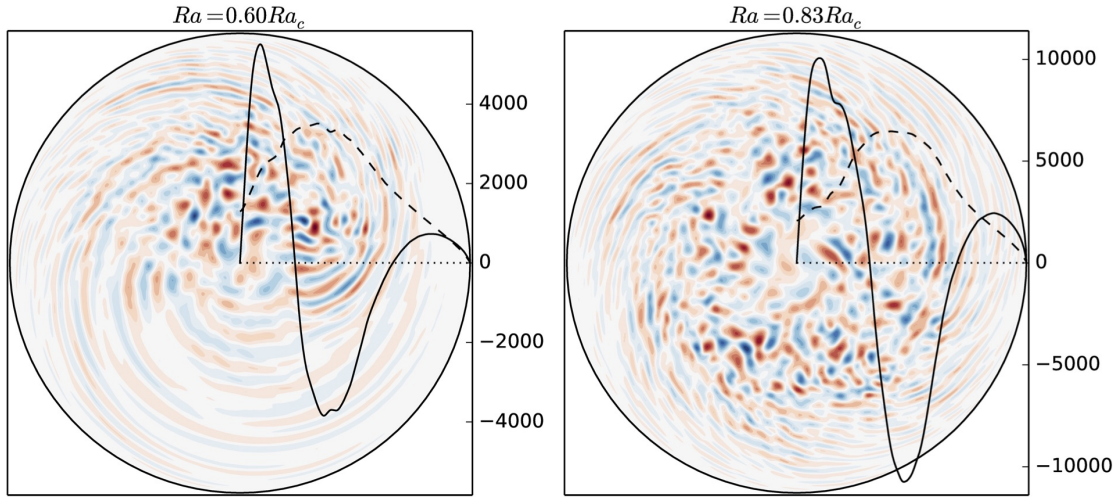


(a) (b)

Figure 6: Streamfunction (colour, snapshot) and radial profiles of $U_s$ (dashed line) and $U_0$ (solid line) (time averages) for $Ek = 10^{-8}$, $Pr = 10^{-2}$: (a) $Ra = Ra_s = 0.60 Ra_c$ and (b) $Ra = 0.83 Ra_c$.

Rayleigh number, $Ra_s$, where the convection abruptly shuts down. At $Ra = Ra_s$, the value of $Re$ is discontinuous: for Rayleigh numbers above $Ra_s$, we have $Re > 5000$, whereas for all $Ra$ below $Ra_s$, $Re = 0$. This behaviour ($Ra_s < Ra_c$) is typical of a subcritical onset of nonlinear convection. For $Ek = 10^{-8}$ and $Pr = 10^{-2}$, we find that $Ra_s/Ra_c = 0.60$. Figures 6(a)-6(b) show snapshots of the streamfunction for $Pr = 10^{-2}$ and two Rayleigh numbers on the subcritical branch, $Ra/Ra_c = 0.60$ and 0.83. For $Ra = Ra_s = 0.60 Ra_c$, the convective flow is similar to the saturated case described previously in figure 4(c). The main difference is that the amplitude of the flow in the inner convective region is concentrated in a localised structure, that drifts in the azimuthal direction with time. The localisation of the convection might indicate that the system struggles to maintain convection for this Rayleigh number. However the kinetic energy of the convective and zonal flows do not decay during the entire time integration of the simulation, which corresponds to 200 convective turnover timescales (where one turnover timescale is calculated as $1/Re_c$), or equivalently, 2 global thermal diffusion timescales. For larger Rayleigh numbers, the localisation in the inner convective region disappears and the convection fills all longitudes, as observed for $Ra = 0.83 Ra_c$ in figure 6(b). The radial profile $U_s$ is plotted in figures 6(a)-6(b). The rms radial velocity peaks in the inner convective region, and then, monotonically decreases in the outer Rossby wave region. The boundary between the convective inner region and the outer Rossby wave region moves outwards when $Ra$ increases. The radial profile of the zonal flow, $U_0$, is also plotted in figures 6(a)-6(b). As described in the saturated case of figure 4(c), the zonal flow displays three jets in both cases. The peak of the middle retrograde jet roughly coincides with the maximum of $U_s$. The zonal flows represent a significant portion of the total flow with the amplitude of $Re_0$ increasing from $0.5 Re_c$ to $1.3 Re_c$ when $Ra/Ra_c$ varies from 0.60 to 3. No significant change in the flow is observed when the Rayleigh number is varied across the linear critical value $Ra_c$, and all of the output parameters evolve continuously, similarly to $Re_c$ in figure 5(a). No continuous branch of convection is found at $Ra = Ra_c$ when the convection is started from a small perturbation as described for $Ek = 10^{-5}$.

Within the interval $Ra_s \leq Ra < Ra_c$, the system has two stable solutions: one is

| $Ek$ | $10^{-8}$ | $10^{-8}$ | $10^{-8}$ | $10^{-7}$ |
|---|---|---|---|---|
| $Pr$ | $10^{-1}$ | $10^{-1.5}$ | $10^{-2}$ | $10^{-2}$ |
| $Ra_s/Ra_c$ | 0.96 | 0.84 | 0.60 | 0.73 |

Table 1: Values of the ratio of Rayleigh number at the nonlinear onset of convection to the critical Rayleigh number at the linear onset in the subcritical cases.

located on the subcritical branch shown in red in figure 5(a) and is found by using an initial condition with a large enough amplitude; the other solution corresponds to $Re = 0$ and is found by starting the simulation from a small perturbation. In order to quantify how large the finite amplitude of the initial condition must be to access the subcritical branch, we perform a series of simulations where the initial condition is taken from a snapshot of the saturated solution on the subcritical branch for given parameters and we initially divide the amplitude of the velocity by a given factor. By a trial and error procedure, we determine the factor that separates a solution where the kinetic energy decays to zero from a solution where the kinetic energy grows back to the value on the subcritical branch. The limit between the values of $Re^*$ of the initial condition leading to either the decaying solution or the growing solution are shown in figure 5(a). As expected, we find that for values of $Ra$ just above $Ra_s$, the finite amplitude of the initial condition must be much larger than for values of $Ra$ just below $Ra_c$.

By varying the Prandtl number between $[10^{-2}, 10^{-1}]$ and the Ekman number between $[10^{-8}, 10^{-5}]$, we find that subcritical convection occurs for $Ek = 10^{-8}$ at $Pr \leq 10^{-1}$ and $Ek = 10^{-7}$ at $Pr \leq 10^{-2}$. Table 1 gives the values of $Ra_s/Ra_c$ for the subcritical cases and figure 5(b) shows $Re$ as a function of $Ra/Ra_c$ for these cases. Note that long time integrations are required to determine $Ra_s$. The values of $Ra_s$ are obtained from simulations where the convection does not decay for the entire duration of the calculation, which is at least 200 convective turnover timescales. We find that the value of $Re$ at $Ra = Ra_s$ is of the order of or larger than $10^3$. The ratio $Ra_s/Ra_c$ decreases when $Ek$ decreases, and also when $Pr$ decreases. Consequently, our results suggest that the subcritical behaviour is amplified by low Ekman and Prandtl numbers.

The subcritical behaviour of convection in internal heating models in the limit of small $Ek$ was anticipated from the work of Soward (1977), who found weakly nonlinear solutions close to the critical Rayleigh number at the linear onset predicted by the local theory of Busse (1970), which is significantly smaller than the true global value (Jones *et al.*, 2000). These nonlinear solutions are maintained in the subcritical domain because the zonal shear produced by nonlinear effects opposes the process of phase mixing, which is responsible for the decay of the linear solution. Subcritical convection for small Ekman numbers was also predicted by Plaut *et al.* (2008) from a weakly nonlinear analysis of a quasi-geostrophic model with internal heating. Plaut *et al.* found that the bifurcation to the thermal Rossby waves changes from supercritical to subcritical for $Ek \leq 6.7 \times 10^{-7}$ (in our scaling) at $Pr = 1$. Their analysis demonstrates that the nonlinearities in the temperature equation are responsible for the transition. These nonlinearities are produced by the interactions of the zonal flow with the temperature perturbation of the wave and by the interactions of the axisymmetric temperature with the velocity of the wave. The difference between our numerical results and the weakly nonlinear analysis of Plaut *et al.*, which predicts subcriticality for larger $Ek$ at $Pr = 1$, is possibly due to their treatment of the temperature in 2D. As far as we know, the numerical results of the present paper are the first to demonstrate the existence of subcritical rotating convection in a fully

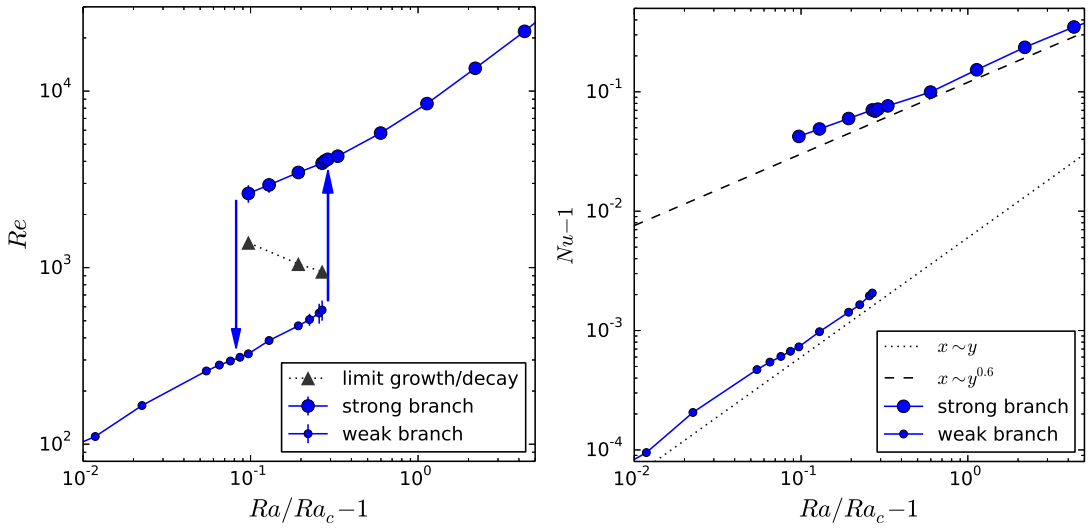


Figure 7: Evolution of (a) $Re$ and (b) $Nu-1$ as a function of the Rayleigh number for $E=10^{-6}$ and $Pr=10^{-2}$.

nonlinear model in spherical geometry. The requirements of small Ekman numbers and small Prandtl numbers (at least for $Ek \in [10^{-8}, 10^{-7}]$) can explain why subcriticality has not been observed in previous numerical models (e.g. by Morin & Dormy (2004) with QG simulations at $Ek = 2\times10^{-7}$ and $Pr=1$). Although subcriticality in the fully 3D system has been predicted from the work of Soward (1977) for small $Ek$, its presence in our results might yet be a consequence of our quasi-geostrophic approximation. Future 3D simulations will be needed to determine whether this is the case.

### 3.3 A hysteresis loop for $E=10^{-6}$ and $Pr=10^{-2}$

For $Ek=10^{-6}$, the bifurcation at the onset of convection is supercritical for all the Prandtl numbers studied here ($Pr \in [10^{-2}, 10^{-1}]$). For $Pr=10^{-2}$, we observe an interesting behaviour near the onset: two stable branches of convection co-exist within a limited range of Rayleigh numbers. This behaviour can be seen in the evolution of $Re$ and $Nu-1$ with $Ra/Ra_c-1$ in figure 7. On the upper branch, $Re$ is one order of magnitude larger than on the lower branch. We thus refer to the upper branch as strong and the lower branch as weak. The two branches are stable and co-exist for Rayleigh numbers between $1.09 \leq Ra/Ra_c \leq 1.27$. The co-existence of two stable branches for a range of $Ra$ leads to a hysteresis loop. The convection selects the weak or the strong branch depending on the dynamical history of the system. For instance, the system remains on the strong branch if the initial condition is taken from a simulation with $Ra > 1.27Ra_c$ and $Ra$ is then decreased down to $1.09Ra_c$. For $Ra > 1.27Ra_c$, only the strong branch exists according to our calculations. When the system is located on the weak branch, an increase of the Rayleigh number above $1.27Ra_c$ therefore leads the system to jump to the strong branch.

In order to quantify the amplitude of the velocity required to jump from one branch to the other, we follow the same numerical procedure as described in §3.2. As an initial condition, we use a snapshot of a solution on the weak branch that we multiply by a given factor and determine the initial amplitude of the flow leading to either a return to the weak branch or a growth to the strong branch. The triangles in figure 7(a) indicate the limit between the initial value of the rms velocity leading to the growth or the decay of

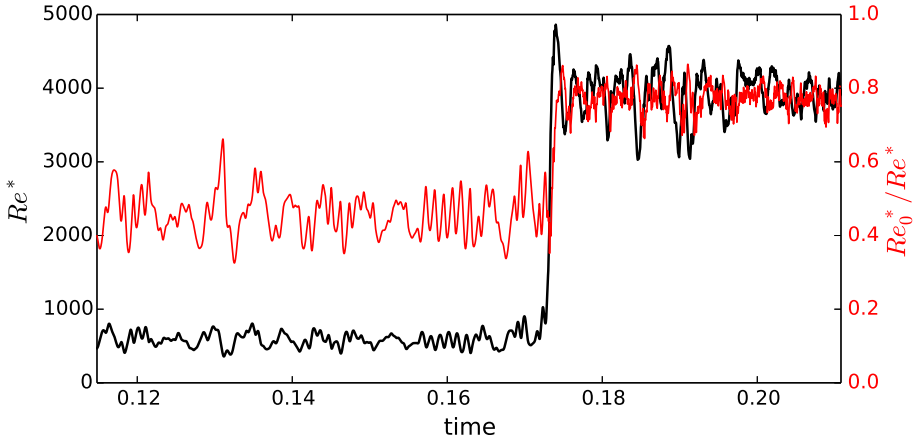


Figure 8: Time series of $Re^*$ (thick black line, left axis) and $Re_0^*/Re^*$ (red, right axis) for a simulation near the edge of the hysteresis loop $E = 10^{-6}$, $Pr = 10^{-2}$ and $Ra = 1.27Ra_c$.

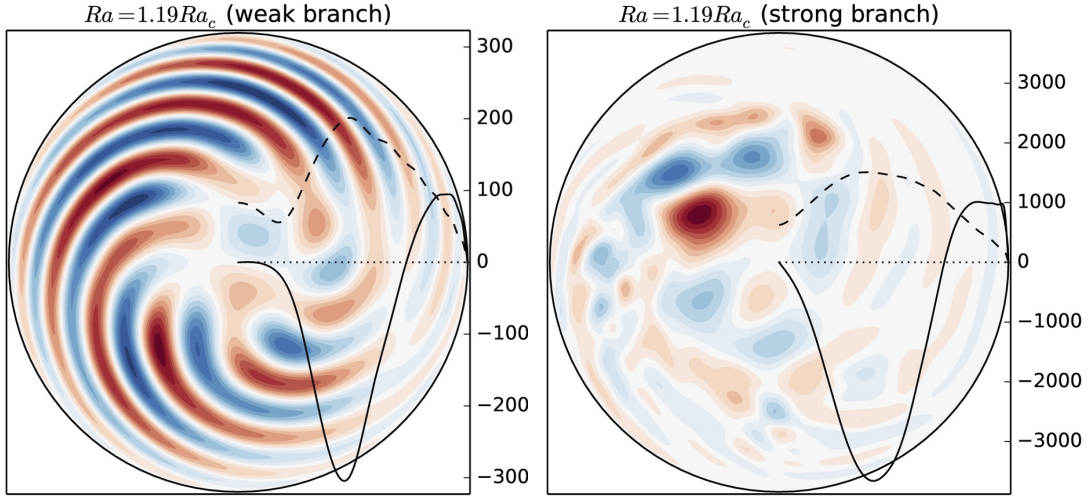


Figure 9: Streamfunction (colour), $U_0$ (solid line) and $U_s$ (dashed line) for $Ek = 10^{-6}$, $Pr = 10^{-2}$ and $Ra = 1.19Ra_c$ on (a) the weak branch and (b) the strong branch.

the energy. As expected a larger amplitude of the initial velocity is required to jump to the strong branch for $Ra = 1.09Ra_c$ than $Ra = 1.27Ra_c$. In fact, for $Ra = 1.27Ra_c$, we observe that, when the system is on the weak branch, a fluctuation of the kinetic energy can lead the system to jump to the strong branch regime. Figure 8 shows this jump in a time series of the Reynolds number, $Re^*$. The two branches are well separated as there is no slow variation on the weak branch towards the strong branch, but only a sudden jump that lasts less than 3 convective turnover timescales. The ratio of zonal to total Reynolds numbers (plotted according to the right axis) is approximately 0.45 on the weak branch and increases to approximately 0.8 after the jump to the strong branch.

Typical convective flows on the weak and strong branches are shown in figures 9(a)-9(b) for the same Rayleigh number $Ra = 1.19Ra_c$. On the weak branch, the flow consists in thermal Rossby waves. The zonal flow has a double jet structure and its amplitude is comparable to the amplitude of the radial flow. The characteristics of this flow are similar to the case described near the onset of convection for $Ek = 10^{-5}$ (§3.1). On the strong

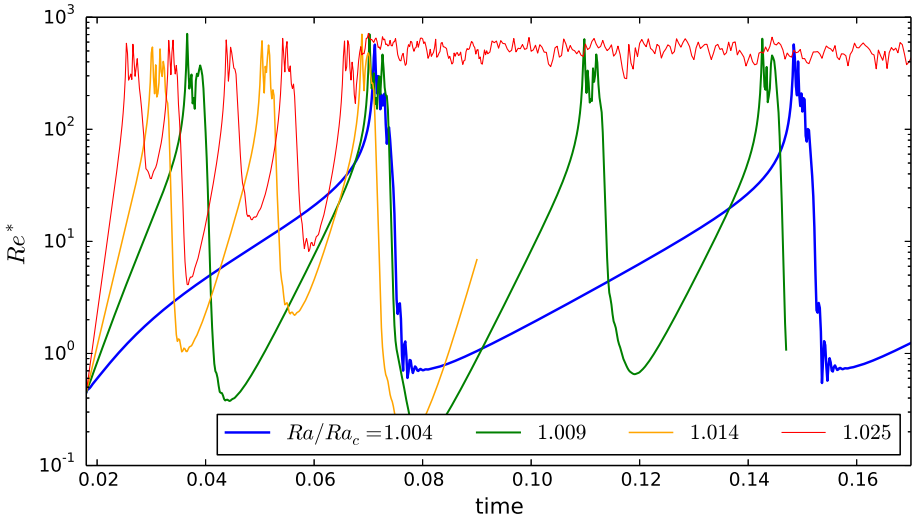


Figure 10: Time series of the Reynolds number, $Re^*$, for $E = 10^{-7}$ and $Pr = 10^{-1}$ and Rayleigh numbers near the onset.

branch, the thermal Rossby waves are not visible anymore and a wide range of lengthscales are observed. The zonal flow has a larger amplitude than the radial velocity. Not only do the solutions look different on the two branches, the global properties of the convection also follow different scaling laws with the input parameters. The evolution of $Nu$ with the Rayleigh number (figure 7(b)) is less steep on the strong branch compared with the weak branch. On the weak branch we find that the points approximately follow a power law $Nu \sim (Ra/Ra_c - 1)^\alpha$ with $\alpha = 1$, whereas on the strong branch $\alpha = 0.6$.

### 3.4 Non-linear oscillations for $E = 10^{-7}$ and $Pr = 10^{-1}$

For $E = 10^{-7}$ and $Pr = 10^{-1}$, we observe an interesting behaviour between the linear onset of convection and the saturated branch of convection, for values of $Ra$ between $Ra_c$ and $1.025Ra_c$. This behaviour is best observed in the time series of $Re^*$ shown in figure 10 for Rayleigh numbers in this interval. $Re^*$ first grows at a rate that depends on $Ra$ and then reaches a value of approximately 400. After a few fluctuations around this mean value, $Re^*$ decreases rapidly. The system subsequently enters a new growing phase and the oscillation repeats itself. The duration of the oscillation depends on the growth rate, and so, larger Rayleigh numbers have shorter period. For $Ra = 1.025Ra_c$, the system eventually stays on the saturated branch after a few oscillations, after which it never goes back to the oscillating phase.

This behaviour is similar to nonlinear oscillations such as relaxation oscillations found in many dynamical systems (Fauve, 1998). These oscillations are quasi-periodic and may be better understood using phase diagrams. Figure 11(a) shows the phase diagram of the ratio of the zonal to convective Reynolds numbers, $Re_0^*/Re_c^*$, versus the convective Reynolds number, $Re_c^*$, for the same time series as figure 10. Figure 11(b) shows the phase diagram for the rms axisymmetric temperature, $\Theta_0^*$, versus $Re_c^*$. During the exponential growing phase $Re_c^*$ (labelled (A)), all trajectories follow the same path and $Re_0^*$ increases as the square of $Re_c^*$, in agreement with weakly nonlinear analysis near the onset of convection (see §3.1). The system reaches a maximum (B), where $Re_0^*$ has a similar amplitude to $Re_c^*$. A dissipative phase (C) then follows during which $Re_0^*$ and $Re_c^*$ initially decay at the same rate. The three quantities, $Re_c^*$, $Re_0^*$ and $\Theta_0^*$, all start to decay at the same

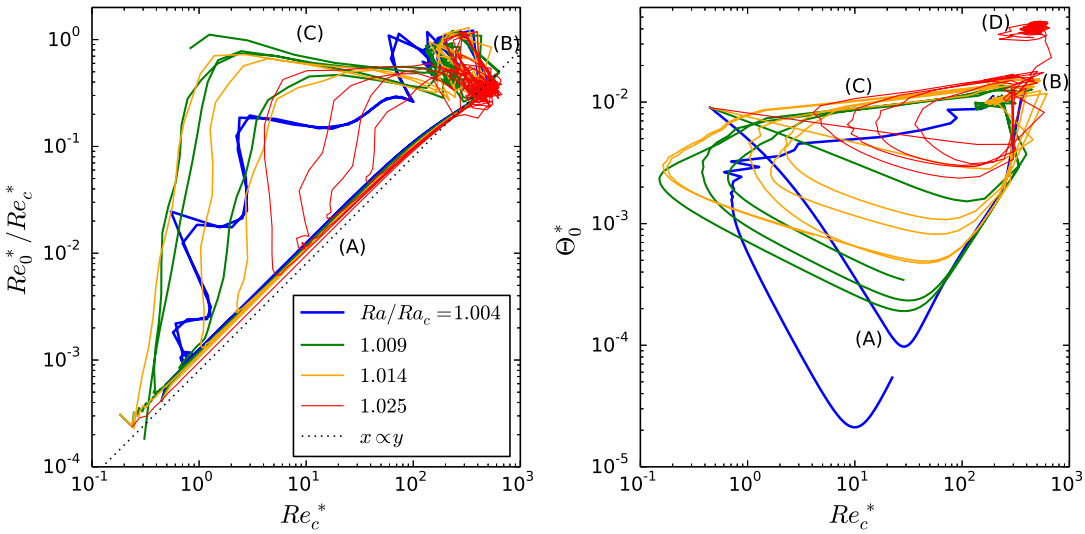


Figure 11: Phase diagram of (a) $Re_0^*/Re_c^*$ versus $Re_c^*$ and (b) $\Theta_0^*$ versus $Re_c^*$ for the same time series as figure 10.

time. While $Re_c^*$ and $Re_0^*$ enter together the growing phase (A), the decay of $\Theta_0^*$ persists for longer. The three phases (A, B, C) are fairly similar for all the Rayleigh numbers, although the system can follow different trajectories during the dissipative phase. For the largest Rayleigh number ($Ra = 1.025Ra_c$), the system exits the oscillating regime to reach a stagnation point (D), which is clearly distinct from the phase (B) according to the measurements of $\Theta_0^*$. During the phase (D), the characteristics of the flow are similar than the ones described in §3.2 for $Ek = 10^{-8}$, so this saturated regime corresponds to the strong branch of convection.

Relaxation oscillations are a well-known phenomenon in rotating spherical convection for Rayleigh numbers a few times above onset (e.g. Grote & Busse, 2001; Morin & Dormy, 2004; Teed *et al.*, 2012). However, unlike in these higher $Ra$ relaxation oscillations, which are caused by the disruption of the convection by the zonal flow and the axisymmetric temperature gradient (Teed *et al.*, 2012), we do not observe here a time lag between the maximum of $Re_0^*$ and $Re_c^*$, so the oscillations of figure 10 are produced by a different mechanism.

Figure 12 shows a series of snapshots of the streamfunction (colour) and the zonal flow (solid black line) during the different phases of the nonlinear oscillation for $Ra = 1.004Ra_c$. During the growing phase (A) ($t = 0.076$), the flow consists of a thermal Rossby wave and a double zonal jet, both developing around the radius $s = 0.5$, reminiscent of the solution on the weak branch. When the system reaches the maximum (B) ($t = 0.078$), the thermal Rossby wave and the zonal flow drift inwards. A narrow prograde zonal jet starts to develop around $s = 0.35$ ($t = 0.0781$) and rapidly gains a very large amplitude ($t = 0.0783$). The non-axisymmetric flow is maximum inside the narrow newly formed prograde jet and keeps the same azimuthal wavenumber as the thermal Rossby wave. The amplitude of both the zonal and non-axisymmetric flows then decays rapidly (phase (C)). A new oscillation begins with the growth of a thermal Rossby wave and its associated double zonal jet around the radius $s = 0.5$, while the zonal flow of the past oscillation finishes to be dissipated ($t = 0.082$). The inward migration of the non-axisymmetric and zonal flows during the phase (B) is probably the cause for the disruption of the convection and

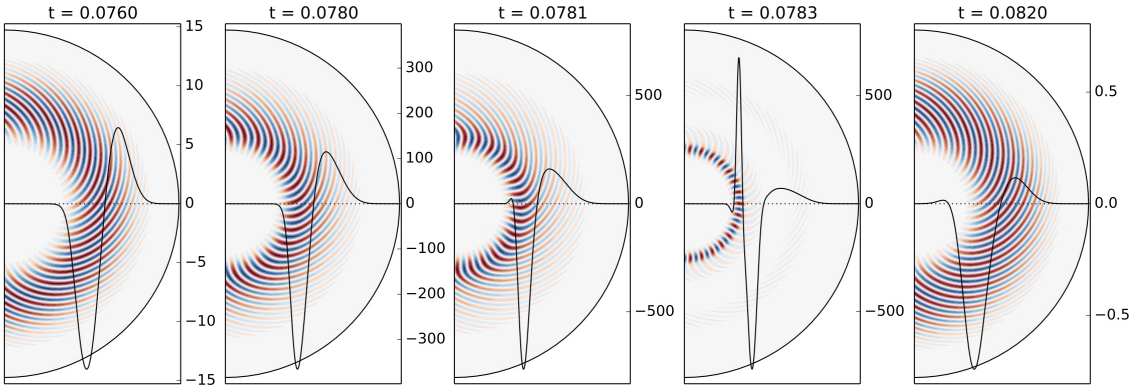


Figure 12: Snapshots of the streamfunction and the zonal flow for $E = 10^{-7}$, $Pr = 0.1$ and $Ra = 1.004Ra_c$. Between the first and last snapshots, a time corresponding to approximately $10^4$ rotation periods has elapsed.

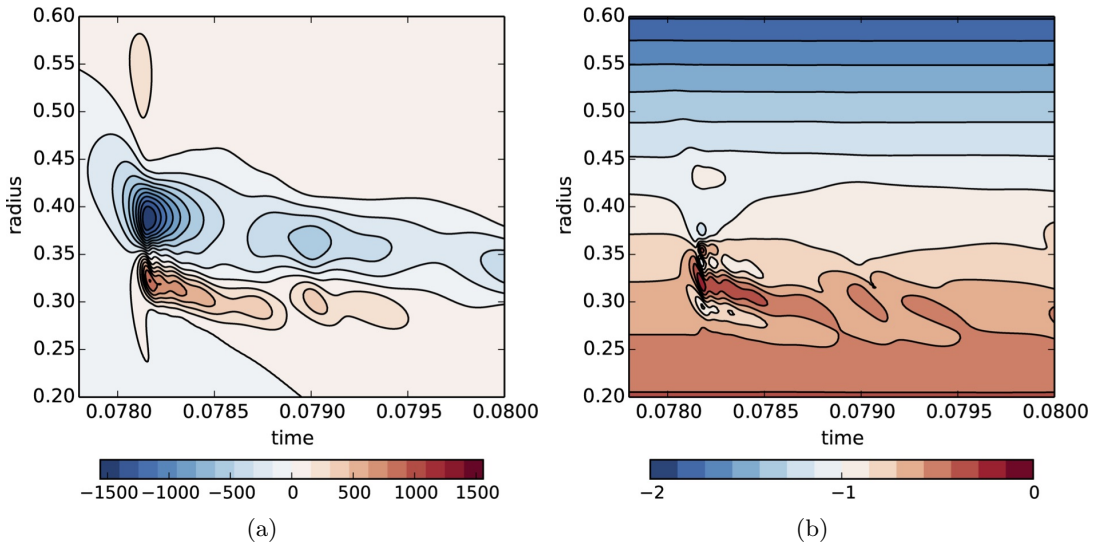


Figure 13: Space-time diagram of (a) $\overline{u_\phi}$ and (b) $\Delta$ for $E = 10^{-7}$, $Pr = 0.1$ and $Ra = 1.004Ra_c$.

the oscillatory behaviour. The mechanism responsible for the inward migration remains unclear as the competitive effects that either inhibit ($\beta$ effect) or promote (gravity along $s$) convection depend on radius.

We note that a secondary effect might arise from the inward migration of the zonal flow in the form of a shear instability. Indeed, the Rossby wave that is confined within the intense narrow prograde jet ($t = 0.0783$ in figure 12) could have been excited by such an instability. A sufficient and necessary condition for the barotropic instability of a shear flow in a inviscid Boussinesq fluid is that the quantity $\Delta = 2\beta Ek^{-1} - d\overline{\zeta}/ds$, where $\overline{\zeta} = d\overline{u_\phi}/ds + \overline{u_\phi}/s$, changes sign at some radius (Kuo, 1949; Ingersoll & Pollard, 1982). Guervilly *et al.* (2012) showed that the threshold of the instability obtained with numerical simulations at finite $Ek$ approaches asymptotically the inviscid theoretical prediction as the Ekman number is decreased and a good quantitative agreement is obtained at $Ek = 10^{-7}$. Figure 13 shows the space-time diagram of $\overline{u_\phi}$ and $\Delta$ between the time $t = 0.0778$ and $t = 0.08$ for the same simulation as figure 12. $\Delta$ is always negative, although it comes close

to zero when the narrow prograde jet is at its maximum. It is nonetheless possible that the linear stability criteria is violated, but this cannot be strictly identified in the nonlinear simulation because the zonal flow would be rapidly modified by the growth of the shear instability. We emphasize that if the zonal flow is shear unstable, it is a secondary effect and not the cause of the inward migration.

We find similar nonlinear oscillations in the vicinity of the linear onset of convection for $Ek = 10^{-6}$ and $Pr = 10^{-1}$, but in a narrower window of Rayleigh numbers (between $Ra = Ra_c$ and $Ra = 1.0015 Ra_c$). For larger Rayleigh numbers, the convection is similar to the solution found on the weak branch with thermal Rossby waves. This therefore indicates that the nonlinear oscillations are not a consequence of the existence of a strong branch of convection.

# 4 Discussion

We have studied rotating thermal convection driven by internal heating in a full sphere near the onset of convection for values of the Prandtl number relevant for liquid metals ($Pr \in [10^{-2}, 10^{-1}]$) and low Ekman numbers ($Ek \in [10^{-8}, 10^{-5}]$). We have used an hybrid numerical model that couples a quasi-geostrophic approximation for the velocity to a fully 3D temperature field. The model includes Ekman pumping to mimic no-slip boundary conditions. Our main finding is the identification of two distinct branches of rapidly-rotating convection: (i) a weak branch for $Ek \geq O(10^{-6})$ that is linked to the linear onset of convection (at $Ra = Ra_c$) by a supercritical bifurcation and (ii) a strong branch for lower Ekman numbers that is discontinuous at the onset and can only be reached by using finite amplitude perturbations as initial conditions. On the weak branch for $Ra$ just above $Ra_c$, the flow consists of the interaction of thermal Rossby waves and a zonal flow with a double jet structure, and has been extensively documented in the literature (e.g. Busse & Hood, 1982; Zhang, 1992). The amplitude of the zonal flow on this branch near onset is smaller than the amplitude of the convective (i.e. non-axisymmetric) velocity. On the strong branch, the flow contains a wide range of length scales and its Reynolds number $Re$ exceeds $10^3$. The zonal flow has multiple jets for $Ek \leq 10^{-7}$ and its amplitude is comparable to or larger than the convective velocity, even near the nonlinear onset of convection. For $Ek = 10^{-5}$, the transition from quasi-steady convection to time-dependent convection that produces an abrupt kink in the evolution of $Re$ and $Nu$ as a function of $Ra$ (see figures 3(a)-3(b)) corresponds perhaps to the continuous transition from the weak to the strong branch. This transition has been observed in previous 3D models (Tilgner & Busse, 1997; Simitev & Busse, 2003), so the existence of the two branches of convection might not be specific to the quasi-geostrophic model. When the viscous effects become smaller, the transition between the two branches becomes discontinuous leading to the existence of two distinct branches, which allows us to observe a hysteresis loop for $Ek = 10^{-6}$ and $Pr = 10^{-2}$, where the onset of the strong branch occurs at $Ra_s = 1.09 Ra_c$.

For yet lower Ekman numbers, we find that the strong branch becomes subcritical with $Ra_s < Ra_c$. In this case, we did not find the weak branch that is continuous at the linear onset. The parameters $(Ek, Pr)$ for which we observe subcritical convection are denoted by red crosses in the regime diagram shown in figure 14. The ratio $Ra_s/Ra_c$ is indicated next to each point and decreases with the Ekman number and the Prandtl number. To the best of our knowledge, this is the first time that subcriticality is reported in thermal convection in a rotating sphere. It is possible that this behaviour is specific to the quasi-geostrophic model, as the nonlinear bifurcation might be sensitive to the treatment of the axial velocity for instance. Nevertheless subcritical convection in the fully 3D system

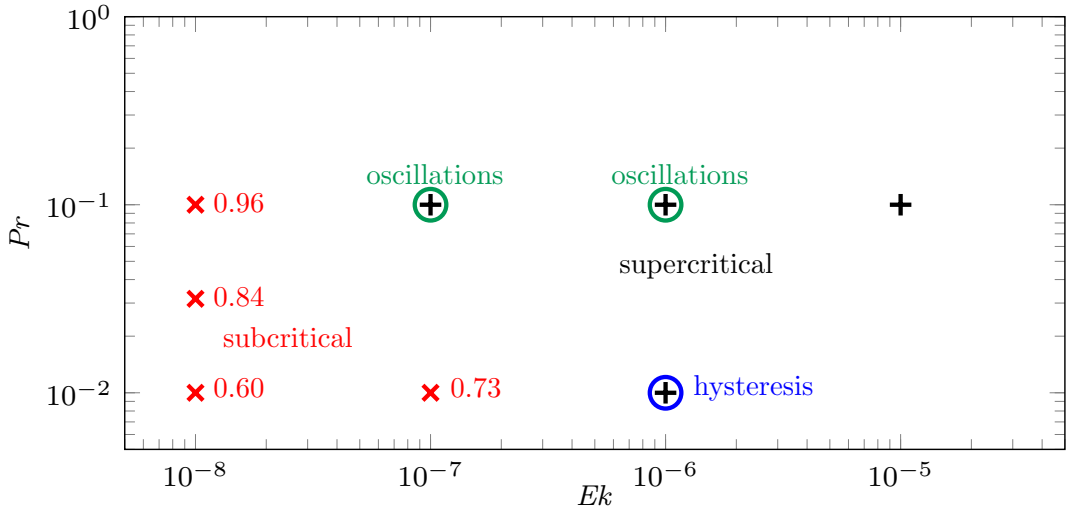


Figure 14: Regime diagram showing the location of the subcritical convection (red cross) and supercritical bifurcation at the onset of nonlinear convection (black plus) identified with our hybrid model. The value annotated next to the subcritical cases gives the ratio $Ra_s/Ra_c$.

has been expected from the work of Soward (1977) in the asymptotic limit $Ek \to 0$ (see figure 3.2 of Proctor (1994)). Soward found that weakly nonlinear solutions exist close to the critical Rayleigh number predicted by the local asymptotic theory, $Ra_c^l$ (Busse, 1970), which is smaller than the critical Rayleigh number of the global asymptotic theory, $Ra_c^g$ (Jones *et al.*, 2000). The discrepancy between local and global asymptotic theories increases at small Prandtl numbers (see Appendix A), so it is perhaps unsurprising that the subcriticality is amplified in this case in our simulations. For $Pr = 10^{-2}$, $Ra_c^l/Ra_c^g = 0.03$, while $Ra_c^l/Ra_c^g = 0.82$ for $Pr = 1$ (Jones *et al.*, 2000). For $Ek = 10^{-8}$ and $Pr = 10^{-2}$, we find that $Ra_s/Ra_c = 0.60$, which could indicate that our simulations are still a long way from the asymptotic limit.

The region of intermediate Ekman numbers, between supercritical bifurcation at $Ek \geq 10^{-5}$ and subcritical convection at $Ek \lesssim 10^{-7}$, displays interesting behaviours such as hysteresis. We also observe nonlinear oscillations for Rayleigh numbers just above the linear onset and up to $Ra/Ra_c = 1.025$ for $Ek = 10^{-7} - 10^{-6}$ and $Pr = 10^{-1}$. For $Ek = 10^{-7}$, the dynamical regime is located on the strong branch for larger Rayleigh numbers, so in this case $Ra_s \approx Ra_c$. For $Ek = 10^{-6}$ however, the solution at larger $Ra$ is similar to the convection at larger Ekman numbers. In both cases, the nonlinear oscillations are due to an inward migration of the convective region, whose cause remains unexplained (see figure 12).

The results presented in this paper rely on a quasi-geostrophic model of the velocity and a 3D model of the temperature, which allowed us to compute small Ekman numbers currently out of reach of 3D models (e.g. Miyagoshi *et al.*, 2010; Yadav *et al.*, 2016; Matsui *et al.*, 2016). Assuming that our results are not specific to the hybrid model, it would be difficult to observe subcriticality for 3D models in the near future, but it might be possible to observe the discontinuous transition between the two branches at low enough Prandtl numbers for $Ek = 10^{-6}$ for instance.

In order to extrapolate the results of numerical models to natural bodies such as the Earth's core, the models must capture the proper convection branch. Indeed here, we find that the scaling of the Nusselt number with the parameters are significantly different on

the weak and strong branches (see figure 7(b) for the hysteresis). In this paper, we do not derive scaling laws for the strong branch for all the studied parameters because it is unclear whether the points actually follow a power law for the small values of $Ra/Ra_c$ studied here. The zonal flows and the scaling of the Reynolds and Nusselt numbers at higher Rayleigh numbers will be addressed in a forthcoming study.

Many questions remain unanswered in our study and, in particular, we have not identified the physical mechanisms leading to subcritical convection in our simulations and controlling the value of $Ra_s$. The zonal flow and/or the axisymmetric temperature are probably essential for the subcriticality (Plaut *et al.*, 2008). Whether the temperature needs to be treated in 3D to observe this behaviour is unclear. The role played by the type of thermal heating also remains an open question. Following the argument that the distinction between the local and global asymptotic theories yields the existence of subcritical convection, Gillet & Jones (2006) argue that the case of differential heating might well always be supercritical because no such distinction exists in this case.

The context of the present work is the study of the fluid dynamics in planetary liquid cores. It is of interest to note that, in this context, the possibility of the subcritical behaviour of rapidly-rotating convection due to the action of a magnetic field is an active area of research (e.g. Sreenivasan & Jones, 2011; Dormy, 2016). In magnetoconvection, where a magnetic field is imposed, the Lorentz force can counteract the inhibiting action of the Coriolis force on the convection and leads to a reduced onset of convection (Chandrasekhar, 1961; Eltayeb, 1972; Fearn, 1979). In dynamo simulations, the magnetic field is sustained by the convective flow and saturates due to the feedback of Lorentz forces on the flow. When a strong magnetic field is sustained, the Lorentz forces can strongly affect the flow and it is then possible that the Rayleigh number required to maintain the dynamo falls below the Rayleigh number required to excite the dynamo in the first place at the dynamo onset (which occurs at $Ra > Ra_c$). Examples of this subcritical behaviour below the dynamo onset have been reported by Kuang *et al.* (2008); Morin & Dormy (2009); Sreenivasan & Jones (2011); Hori & Wicht (2013), and have been used as a possible explanation for the sudden termination of the martian dynamo. However in these examples of convectively-driven dynamos in spherical geometry, the Rayleigh number always exceeds $Ra_c$. As far as we know, the only example of a dynamo simulation operating below $Ra_c$ was found by Stellmach & Hansen (2004) in a planar model of rotating convection. It would be of great interest to study the dynamo action produced by the flows on the strong hydrodynamical branch identified in this paper, and whether the Lorentz force can push the system to remain convective at yet smaller Rayleigh numbers as suggested for instance by Roberts (1988).

## Acknowledgements

CG was supported by the Natural Environment Research Council under grant NE/M017893/1. PC acknowledges the Agence Nationale de la Recherche for supporting this project under grant ANR TuDy. This work was undertaken on ARC1 and ARC2 of the HPC facilities at the University of Leeds, on TOPSY of the HPC facilities at Newcastle University and on the Froggy platform of the CIMENT infrastructure (https://ciment.ujf-grenoble.fr). The CIMENT infrastructure is supported by the Rhône-Alpes region (GRANT CPER07_13 CIRA), the OSUG@2020 labex (reference ANR10 LABX56) and the Equip@Meso project (reference ANR-10-EQPX-29-01). ISTerre is part of Labex OSUG@2020 (ANR10 LABX56). We are grateful to Emmanuel Dormy, Andrew Soward, Toby Wood and the Geodynamo group in Grenoble for helpful discussions and to the

anonymous referees for suggestions that have improved the manuscript.

# A Linear onset of convection

The onset of thermal convection in a rotating sphere with internal heating in the asymptotic limit $Ek \ll 1$ and $Ek/Pr \ll 1$ was studied analytically by Roberts (1968); Busse (1970); Yano (1992); Jones *et al.* (2000). In this limit, the most unstable mode of convection develops in the form of columnar structures aligned with the rotation axis, which are called thermal Rossby waves. They develop around a radius $s \approx 0.5$. Using a local perturbative study, Busse (1970) determined the analytical dependence of the critical parameters at the onset of convection as function of $Ek$ and $Pr$,

$$Ra_c^l = C_r \left(\frac{Pr}{1+Pr}\right)^{4/3} Ek^{-4/3}, \tag{42}$$

$$m_c^l = C_m \left(\frac{Pr}{1+Pr}\right)^{1/3} Ek^{-1/3}, \tag{43}$$

$$\omega_c^l = C_\omega \left(Pr(1+Pr)^2\right)^{-1/3} Ek^{-2/3}, \tag{44}$$

where $Ra_c^l$ is the critical Rayleigh number, $m_c^l$ the marginally stable azimuthal wavenumber, $\omega_c^l$ its frequency, and $C_r$, $C_m$ and $C_\omega$ are constant. However, Soward (1977) showed that small disturbances decay with time for values of the Rayleigh number just above the local critical Rayleigh number (42). Jones *et al.* (2000) calculated the true value of the critical Rayleigh number from the global asymptotic theory, $Ra_c^g$, and found that it is significantly larger than $Ra_c^l$.

In order to benchmark our hybrid model, we have performed calculations with a linearised version of the code and compared the results with the values of the global asymptotic theory of Jones *et al.* (2000) for $Pr \in [10^{-2}, 1]$. We study the onset of the thermal Rossby waves, so we restrict our study to the domain of small Ekman numbers where they are preferred over the equatorially-attached modes, i.e. $Ek \leq 10^{-4}$ for $Pr = 10^{-1}$ and $Ek \leq 10^{-6}$ for $Pr = 10^{-2}$ (see §1). We also compare the dependence of the critical parameters on $Pr$ with the power laws of the local theory (42)-(44). We calculated the linear onset for $Pr = 1$ at $Ek \in [10^{-6}, 10^{-5}]$ to compare our results with published numerical results obtained with a fully 3D model (Dormy *et al.*, 2004) and a quasi-geostrophic description, where the temperature is also treated in 2D (hereafter denoted QG-2D) (Aubert, 2001). In these previous studies, the critical parameters for convection driven by internal heating were only published for $Pr = 1$ and the model includes an inner core of radius 0.35. The boundary conditions for the 3D model of Dormy *et al.* (2004) are no-slip, while the QG-2D model of Aubert (2001) neglects the Ekman pumping.

The critical parameters calculated with our code $(Ra_c, m_c, \omega_c)$ are given in table 2. As the Ekman number is decreased, $Ra_c$ gets closer to the asymptotic value $Ra_c^g$ for all $Pr$. The values of the critical parameters are plotted as a function of $Ek$ in figure 15 for $Pr = 1$. The three critical parameters computed with our hybrid model tend towards the asymptotic values of the global stability analysis when $Ek$ decreases. The critical Rayleigh number of our model is higher than the values obtained with both the 3D and QG-2D models. This is expected because of the stabilising effect of the axial rigidity imposed by the quasi-geostrophic formulation, while the 3D solution keeps a large-scale $z$-dependence (Gillet & Jones, 2006). Furthermore, our hybrid approach includes the axial diffusion of the temperature, which is neglected in the QG-2D model. The $z$-average of the buoyancy force is thus weaker in our hybrid approach, so $Ra_c$ is necessarily larger. The marginally stable

| $Ek$ | $Pr$ | $Ra_c$ | $m_c$ | $\omega_c$ | $Ra_c/Ra_c^g$ |
|---|---|---|---|---|---|
| $10^{-5}$ | 1 | $4.039 \times 10^7$ | 14 | $1.44 \times 10^3$ | 1.68 |
| $10^{-6}$ | 1 | $8.374 \times 10^8$ | 32 | $7.36 \times 10^3$ | 1.61 |
| $10^{-5}$ | $10^{-1}$ | $1.416 \times 10^7$ | 8 | $3.85 \times 10^3$ | 2.14 |
| $10^{-6}$ | $10^{-1}$ | $2.736 \times 10^8$ | 18 | $1.88 \times 10^4$ | 1.92 |
| $10^{-7}$ | $10^{-1}$ | $5.032 \times 10^9$ | 44 | $9.08 \times 10^4$ | 1.64 |
| $10^{-8}$ | $10^{-1}$ | $7.759 \times 10^{10}$ | 109 | $4.73 \times 10^5$ | 1.17 |
| $10^{-6}$ | $10^{-2}$ | $9.389 \times 10^7$ | 9 | $3.95 \times 10^4$ | 1.56 |
| $10^{-7}$ | $10^{-2}$ | $1.818 \times 10^9$ | 20 | $1.90 \times 10^5$ | 1.41 |
| $10^{-8}$ | $10^{-2}$ | $2.962 \times 10^{10}$ | 53 | $8.08 \times 10^5$ | 1.06 |

Table 2: Critical parameters at the linear onset of convection calculated with a linearised version of the hybrid QG-3D numerical code.

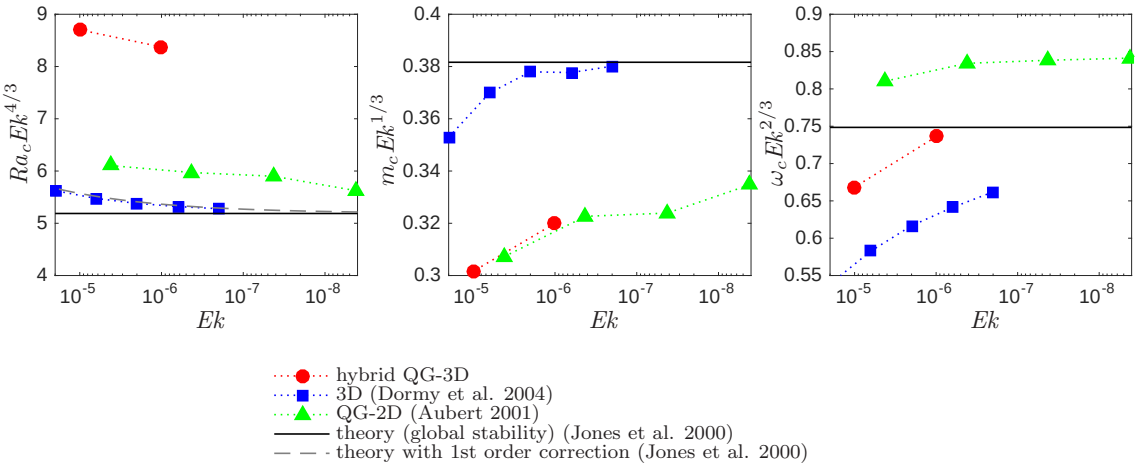


Figure 15: Critical parameters for the linear onset of convection as a function of $Ek$ for $Pr = 1$ computed with our model (hybrid QG-3D), with the 3D model of Dormy *et al.* (2004) and the quasi-geostrophic model of Aubert (2001). These numerical results are compared with the asymptotic results of Jones *et al.* (2000). The dashed gray line represents the asymptotic results including first-order correction (Jones *et al.*, 2000).

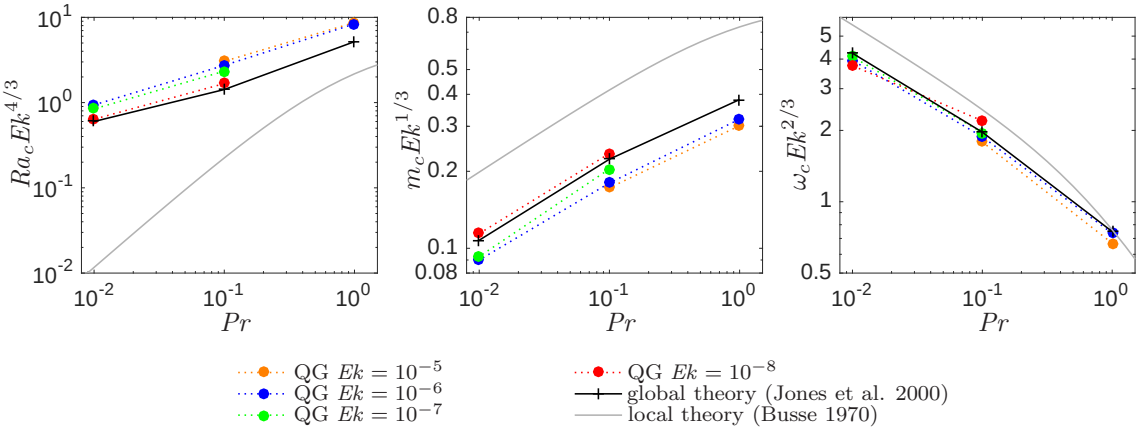


Figure 16: Critical parameters for the linear onset of convection as a function of $Pr$ computed with our hybrid QG model and compared with the asymptotic results of Jones *et al.* (2000) (global theory) and Busse (1970) (local theory).

mode $m_c$ is smaller in our hybrid model compared with the asymptotic results. Again, this is consistent with the axial rigidity of the quasi-geostrophic flow, which requires the convection to first develop at a slightly smaller critical radius, thereby selecting a smaller $m_c$.

The critical parameters $(Ra_c, m_c, \omega_c)$ are plotted as a function of $Pr$ in figure 16. Our hybrid model follows well the trend of the global asymptotic theory for the three critical parameters. Convection at smaller $Pr$ develops on larger scales at the onset. Accordingly, the critical frequency is larger (e.g. Jones, 2007). These results agree reasonably well with the trends given by the power laws of the local theory for $m_c^l$ and $\omega_c^l$ ((43)-(44)) when $Pr < 0.1$, but the prefactors differ significantly. The critical Rayleigh number given by both our numerical results and the global asymptotic results differs greatly from the prediction of the local theory ($Ra_c^l \propto Pr^{4/3}$ when $Pr \ll 1$), as already observed by Zhang (1992). The discrepancy with $Ra_c^l$ (42) increases as the Prandtl number decreases: the difference between local and global critical Rayleigh number is nearly two orders of magnitude for $Pr = 10^{-2}$. Zhang (1992) attributed this discrepancy to the tilt of the thermal Rossby waves, which is more pronounced for small $Pr$.

## References


Ardes, M., Busse, F. H. & Wicht, J. 1997 Thermal convection in rotating spherical shells. *Phys. Earth Planet. Inter.* **99**, 55–67.

Aubert, J. 2001 Modèles expérimentaux et numériques de la convection dans le noyau terrestre. PhD thesis, Université Joseph Fourier Grenoble.

Aubert, J., Gillet, N. & Cardin, P. 2003 Quasigeostrophic models of convection in rotating spherical shells. *Geochemistry Geophysics Geosystems* **4** (7), 1052.

Aurnou, J.M., Calkins, M.A., Cheng, J.S., Julien, K., King, E.M., Nieves, D., Soderlund, K.M. & Stellmach, S. 2015 Rotating convective turbulence in Earth and planetary cores. *Phys. Earth Planet. Int.* **246**, 52–71.

Bajaj, K.M.S., Ahlers, G. & Pesch, W. 2002 Rayleigh-Bénard convection with rotation at small Prandtl numbers. *Phys. Rev. E* **65** (5), 056309.

Brummell, N. H. & Hart, J. E. 1993 High Rayleigh number -convection. *Geophys. Astrophys. Fluid Dyn.* **68**, 85–114.

Busse, F. H. 1970 Thermal instabilities in rapidly rotating systems. *J. Fluid Mech.* **44**, 441–460.

Busse, F. H. & Hood, L. L. 1982 Differential rotation driven by convection in a rapidly rotating annulus. *Geophys. Astrophys. Fluid Dyn.* **21** (1-2), 59–74.

Busse, F. H. & Or, A. C. 1986 Convection in a rotating cylindrical annulus - thermal Rossby waves. *J. Fluid Mech.* **166**, 173–187.

Busse, F. H. & Simitev, R. 2004 Inertial convection in rotating fluid spheres. *J. Fluid Mech.* **498**, 23–30.

Calkins, M.A., Aurnou, J.M., Eldredge, J.D. & Julien, K. 2012 The influence of fluid properties on the morphology of core turbulence and the geomagnetic field. *Earth Planet. Sci. Lett.* **359**, 55–60.

Cardin, P. & Olson, P. 1994 Chaotic thermal convection in a rapidly rotating spherical shell: consequences for flow in the outer core. *Phys. Earth Planet. Inter.* **82**, 235–259.

Carrigan, C. R. & Busse, F. H. 1983 An experimental and theoretical investigation of the onset of convection in rotating spherical shells. *J. Fluid Mech.* **126**, 287–305.

Chandrasekhar, S. 1961 *Hydrodynamic and hydromagnetic stability*. Oxford: Clarendon.

Christensen, U. R. 2002 Zonal flow driven by strongly supercritical convection in rotating spherical shells. *J. Fluid Mech.* **470**, 115–133.

Clever, R.M. & Busse, F. H. 2000 Convection in a low Prandtl number fluid layer rotating about a vertical axis. *European Journal of Mechanics-B/Fluids* **19** (2), 213–227.

Cordero, S. & Busse, F. H. 1992 Experiments on convection in rotating hemispherical shells: Transition to a quasi-periodic state. *Geophys. Res. Lett.* **19** (8), 733–736.

Costa, L.D., Knobloch, E. & Weiss, N.O. 1981 Oscillations in double-diffusive convection. *J. Fluid Mech.* **109** (257), 25–43.

Dormy, E. 2016 Strong-field spherical dynamos. *J. Fluid Mech.* **789**, 500–513.

Dormy, E., Soward, A. M., Jones, C. A., Jault, D. & Cardin, P. 2004 The onset of thermal convection in rotating spherical shells. *J. Fluid Mech.* **501**, 43–70.

Eltayeb, I.A. 1972 Hydromagnetic convection in a rapidly rotating fluid layer. *Proc. R. Soc. Lond. A* **326** (1565), 229–254.

Fauve, S. 1998 Pattern forming instabilities. In *Hydrodynamics and non linear instabilities* (ed. C. Godrèche & P. Manneville), pp. 387–489. Cambridge University Press.

Fearn, D. R. 1979 Thermal and magnetic instabilities in a rapidly rotating fluid sphere. *Geophys. Astrophys. Fluid Dyn.* **14** (1), 103–126.

Gillet, N., Brito, D., Jault, D. & Nataf, H.-C. 2007 Experimental and numerical study of convection in a rapidly rotating spherical shell. *J. Fluid Mech.* **580**, 83–121.

Gillet, N. & Jones, C. A. 2006 The quasi-geostrophic model for rapidly rotating spherical convection outside the tangent cylinder. *J. Fluid Mech.* **554**, 343–369.

Goluskin, D. 2016 *Internally heated convection and Rayleigh-Bénard convection*. Springer.

Greenspan, H. P. 1968 *The theory of rotating fluids*. Cambridge: University Press.

Grote, E. & Busse, F. H. 2001 Dynamics of convection and dynamos in rotating spherical fluid shells. *Fluid Dyn. Res.* **28**, 349–368.

Guervilly, C., Cardin, P. & Schaeffer, N. 2012 A dynamo driven by zonal jets at the upper surface: Applications to giant planets. *Icarus* **218**, 100–114.

Hori, K. & Wicht, J. 2013 Subcritical dynamos in the early Mars' core: Implications for cessation of the past Martian dynamo. *Phys. Earth Planet. Inter.* **219**, 21–33.

Ingersoll, A. P. & Pollard, D. 1982 Motion in the interiors and atmospheres of Jupiter and Saturn - Scale analysis, anelastic equations, barotropic stability criterion. *Icarus* **52**, 62–80.

Jones, C. A. 2007 Thermal and compositional convection in the outer core. In *Treatise on Geophysics* (ed. Gerald Schubert), pp. 131 – 185. Amsterdam: Elsevier.

Jones, C. A., Rotvig, J. & Abdulrahman, A. 2003 Multiple jets and zonal flow on Jupiter. *Geophys. Res. Lett.* **30** (14), 140000.

Jones, C. A., Soward, A. M. & Mussa, A. I. 2000 The onset of thermal convection in a rapidly rotating sphere. *J. Fluid Mech.* **405**, 157–179.

King, E.M. & Aurnou, J.M. 2013 Turbulent convection in liquid metal with and without rotation. *Proceedings of the National Academy of Sciences* **110** (17), 6688–6693.

Kuang, W., Jiang, W. & Wang, T. 2008 Sudden termination of Martian dynamo?: Implications from subcritical dynamo simulations. *Geophys. Res. Lett.* **35**.

Kuo, H.-L. 1949 Dynamic instability of two-dimensional nondivergent flow in a barotropic atmosphere. *J. Atmos. Sci.* **6**, 105–122.

Labbé, F, Jault, D & Gillet, N 2015 On magnetostrophic inertia-less waves in quasi-geostrophic models of planetary cores. *Geophys. Astrophys. Fluid Dyn.* **109** (6), 587–610.

Manneville, P. 2004 *Instabilities, Chaos and Turbulence*. Imperial College Press.

Matsui, H., Heien, E., Aubert, J., Aurnou, J. M., Avery, M., Brown, B., Buffett, B. A., Busse, F., Christensen, U. R., Davies, C. J., Featherstone, N., Gastine, T., Glatzmaier, G. A., Gubbins, D., Guermond, J.-L., Hayashi, Y.-Y., Hollerbach, R., Hwang, L. J., Jackson, A., Jones, C. A., Jiang, W., Kellogg, L. H., Kuang, W., Landeau, M., Marti, P. H., Olson, P., Ribeiro, A., Sasaki, Y., Schaeffer, N., Simitev, R. D., Sheyko, A., Silva, L., Stanley, S., Takahashi, F., Takehiro, S.-i., Wicht, J. & Willis, A. P. 2016 Performance benchmarks for a next generation numerical dynamo model. *Geochemistry, Geophysics, Geosystems* **17** (5), 1586–1607.

Miyagoshi, T., Kageyama, A. & Sato, T. 2010 Zonal flow formation in the Earth's core. *Nature* **463**, 793–796.

Morin, V. & Dormy, E. 2004 Time dependent beta-convection in rapidly rotating spherical shells. *Phys. Fluids* **16** (5), 1603–1609.

Morin, V. & Dormy, E. 2009 The dynamo bifurcation in rotating spherical shells. *Int. J. Modern Phys. B* **23**, 5467–5482.

Nataf, H.-C. & Schaeffer, N. 2015 Turbulence in the core. In *Treatise on Geophysics 2nd ed.* (ed. Gerald Schubert), pp. 161–181. Amsterdam: Elsevier.

Olson, P. L. 2013 The new core paradox. *Science* **342** (6157), 431–432.

Or, A. C. & Busse, F. H. 1987 Convection in a rotating cylindrical annulus. II. Transitions to asymmetric and vacillating flow. *J. Fluid Mech.* **174**, 313–326.

Plaut, E. & Busse, F.H. 2002 Low-Prandtl-number convection in a rotating cylindrical annulus. *J. Fluid Mech.* **464**, 345–363.

Plaut, E. & Busse, F.H. 2005 Multicellular convection in rotating annuli. *J. Fluid Mech.* **528**, 119–133.

Plaut, E., Lebranchu, Y., Simitev, R. & Busse, F. H. 2008 On the Reynolds stresses and mean fields generated by pure waves - Applications to shear flows and convection in a rotating shell. *J. Fluid Mech.* **602**, 303–326.

Pozzo, M., Davies, C., Gubbins, D. & Alfe, D. 2012 Thermal and electrical conductivity of iron at Earth/'s core conditions. *Nature* **485** (7398), 355–358.

Proctor, M.R.E. 1994 Convection and magnetoconvection in a rapidly rotating sphere. In *Lectures on solar and planetary dynamos*, p. 97.

Roberts, P.H. 1988 Future of geodynamo theory. *Geophys. Astrophys, Fluid Dyn,* **44** (1-4), 3–31.

Roberts, P. H. 1968 On the thermal instability of a rotating-fluid sphere containing heat sources. *R. Soc. Lond. Phil. Trans. A* **263**, 93–117.

Sánchez, J., Garcia, F. & Net, M. 2016 Critical torsional modes of convection in rotating fluid spheres at high Taylor numbers. *J. Fluid Mech.* **791**, R1.

Scanlon, J.W. & Segel, L.A. 1967 Finite amplitude cellular convection induced by surface tension. *J. Fluid Mech.* **30** (01), 149–162.

Schaeffer, N. & Cardin, P. 2005 Quasigeostrophic model of the instabilities of the Stewartson layer in flat and depth-varying containers. *Phys. Fluids* **17** (10), 104111.

Schaeffer, N. & Cardin, P. 2006 Quasi-geostrophic kinematic dynamos at low magnetic Prandtl number. *Earth Planet. Sci. Lett.* **245**, 595–604.

Schnaubelt, M. & Busse, F.H. 1992 Convection in a rotating cylindrical annulus part 3. vacillating and spatially modulated flows. *J. Fluid Mech.* **245**, 155–173.

Simitev, R. & Busse, F.H. 2003 Patterns of convection in rotating spherical shells. *New Journal of Physics* **5** (1), 97.

Soward, A. M. 1977 On the finite amplitude thermal instability of a rapidly rotating fluid sphere. *Geophys. Astrophys. Fluid Dyn.* **9** (1), 19–74.

Sreenivasan, B. & Jones, C. A. 2011 Helicity generation and subcritical behaviour in rapidly rotating dynamos. *J. Fluid Mech.* **688**, 5.

Stellmach, S. & Hansen, U. 2004 Cartesian convection driven dynamos at low Ekman number. *Phys. Rev. E* **70**, 056312.

Sumita, I. & Olson, P. 2000 Laboratory experiments on high Rayleigh number thermal convection in a rapidly rotating hemispherical shell. *Phys. Earth Planet. Int.* **117**, 153–170.

Sun, Z.-P., Schubert, G. & Glatzmaier, G. A. 1993 Transitions to chaotic thermal convection in a rapidly rotating spherical fluid shell. *Geophys. Astrophys. Fluid Dyn.* **69**, 95–131.

Teed, R.J., Jones, C.A. & Hollerbach, R. 2012 On the necessary conditions for bursts of convection within the rapidly rotating cylindrical annulus. *Phys. Fluids* **24** (6), 066604.

Tilgner, A. & Busse, F.H. 1997 Finite-amplitude convection in rotating spherical fluid shells. *J. Fluid Mech.* **332** (1), 359–376.

Veronis, G. 1966 Motions at subcritical values of the rayleigh number in a rotating fluid. *J. Fluid Mech.* **24** (03), 545–554.

Yadav, R.K., Gastine, T., Christensen, U.R., Duarte, L.D.V. & Reiners, A. 2016 Effect of shear and magnetic field on the heat-transfer efficiency of convection in rotating spherical shells. *Geophys. J. Int.* **204** (2), 1120–1133.

Yano, J.-I. 1992 Asymptotic theory of thermal convection in rapidly rotating systems. *J. Fluid Mech.* **243**, 103–131.

Zhang, K. 1992 Convection in a rapidly rotating spherical shell at infinite prandtl number: transition to vacillating flows. *Phys. Earth Planet. Int.* **72** (3-4), 236–248.

Zhang, K. 1992 Spiralling columnar convection in rapidly rotating spherical fluid shells. *J. Fluid Mech.* **236**, 535–556.

Zhang, K.-K. & Busse, F. H. 1987 On the onset of convection in rotating spherical shells. *Geophys. Astrophys. Fluid Dyn.* **39**, 119–147.

Zhang, K. & Jones, C. A. 1993 The influence of Ekman boundary layers on rotating convection. *Geophys. Astrophys. Fluid Dyn.* **71** (1-4), 145–162.